Prefoldin 5 is a microtubule-associated protein that suppresses Tau-aggregation and neurotoxicity

Anjali Bisht[1], Srikanth Pippadpally[1], Snehasis Majumder[2], Athulya T Gopi[1], Abhijit Das[2], Chandan Sahi[1], Mani Ramaswami[3], Vimlesh Kumar[1*].

[1] Department of Biological Sciences, Indian Institute of Science Education and Research (IISER) Bhopal, Academic Building 3, Bhauri, Bhopal-462 066, Madhya Pradesh, India.

[2] Department of Bioscience and Biotechnology, Indian Institute of Technology Kharagpur, Kharagpur-731302, Midnapore Sadar, India.

[3] Trinity College Institute of Neuroscience (TCIN), University of Dublin 2, Ireland.

* Corresponding author: Tel: +91 755 2691405; Fax: +91 755 2692392; Email- vimlesh@iiserb.ac.in

Running title: Pfdn5 mitigates Tau-induced neurodegeneration

ABSTRACT

Tauopathies represent a major class of neurodegenerative disorders associated with intracellular aggregates of the microtubule-associated protein Tau. To identify molecular modulators of Tau toxicity, we used a genetic screen to identify protein chaperones whose RNAi-mediated knockdown could modulate hTau^{V337M}-induced eye-ommatidial degeneration in *Drosophila*. This screen identified the Prefoldins Pfdn5 and Pfdn6 as strong modifiers of hTau^{V337M} cytotoxicity. Consistent with the known function of Pfdn as a cotranslational chaperone for tubulin, *Pfdn5* mutants showed substantially reduced levels of tubulin monomer. However, additional microtubule-related functions were indicated by the robust unexpected association of Pfdn5 with axonal microtubules *in vivo,* as well as binding with stabilized microtubules in biochemical assays. Loss of Pfdn5 resulted in neuromuscular junctions (NMJ) defects similar to those previously described in hTau-expressing flies: namely, increased supernumerary boutons and fewer microtubule loops within mature presynaptic boutons. Significantly, synaptic phenotypes caused by hTau^{V337M} overexpression were also strongly enhanced in a *Pfdn5* mutant background. Consistent with a role in modulating Tau toxicity, not only did loss of *Pfdn5* result in increased accumulations of Tau-aggregates in hTau^{V337M} expressing neurons, but also neuronal overexpression of Prefoldin strikingly ameliorated age-dependent neurodegeneration and memory deficits induced by pathological hTau. Together, these and other observations described herein: (a) provide new insight into Prefoldin-microtubule interactions; (b) point to essential posttranslational roles for Pfdn5 in controlling Tau-toxicity *in vivo*; and (c) demonstrate that Pfdn5 overexpression is sufficient to restrict Tau-induced neurodegeneration.

Keywords: Neurodegeneration; Tauopathy; Chaperones; Prefoldin; Pfdn5; Microtubules; Synaptic growth; Eye degeneration; *Drosophila*; Learning and memory

INTRODUCTION

Aberrant accumulation of misfolded protein aggregates is associated with neuroinflammation, neuronal death and progressive cognitive decline in diverse groups of neurodegenerative diseases [1-4]. Alzheimer's disease, as well as a subset of other neurodegenerative disorders together referred to as Tauopathies, are defined by accumulated intracellular aggregates of the Tubulin-associated unit (Tau) protein [5-7]. Despite substantial clinical interest and decades of research, therapeutic interventions for treating Tauopathies are still unavailable [4, 8].

Tau is predominantly expressed in neurons, where it stabilizes microtubules, thus facilitating intra-axonal transport [9-11]. Several mutations in Tau protein have been identified that contribute to a wide spectrum of Tauopathies, including Alzheimer's disease, Pick's disease, progressive supranuclear palsy (PSP), corticobasal degeneration (CBD) and frontotemporal dementia with parkinsonism linked to chromosome 17 (FTDP-17) [12, 13]. These pathogenic mutations enhance the propensity for Tau protein hyperphosphorylation at Ser/Thr residues, leading to the formation of neurofibrillary tangles via self-aggregation [14]. The phosphorylated Tau disengages from the microtubule, potentially altering axonal transport and contributing to synapse loss and/or axon retraction [14, 15]. Thus, the self-aggregation of Tau and destabilization of microtubules may contribute to the progression of Tau pathogenesis. Such a model is supported by studies in *Drosophila* and rodent models of Tauopathies. Several of these models of Tauopathy show disrupted microtubules, synaptic abnormalities, and abnormal motor behavior [16]. Significantly, pharmacological stabilization of microtubules or reducing Tau levels can revert at least some of the defects observed in these Tauopathy models [17, 18]. However, alternative approaches to mitigate Tau-induced neurodegeneration are required because the currently available microtubule-targeting drugs are toxic at concentrations required to have an effect in the brain [19]. One approach, suggested by several studies

demonstrating a role for chaperone systems in Tauopathies [20-22], is to identify and manipulate specific molecular chaperones that directly or indirectly control Tau aggregation and Tau-induced neurotoxicity *in vivo* [23, 24].

Molecular chaperones facilitate proper protein folding, prevent protein aggregation and solubilize or facilitate autophagic or proteasomal elimination of protein aggregates [25-27]. Consistent with this, enhanced expression of Hsp70 or HSP90 chaperones in mouse neuroblastoma N2A cells reduces pathological Tau levels by promoting the partitioning of Tau onto microtubules [26]. On the other hand, as chaperones stabilize misfolded protein states, the expression of certain chaperones or cochaperones can sometimes also promote and facilitate the aggregation of Tau [28, 29]. For instance, expression of HSP90 cochaperones, FKBP52 or Aha1 in the mouse brain enhances Tau aggregation, neuroinflammation and cognitive decline in Tau transgenic mouse model [29, 30]. These and other data indicate that: (a) chaperones not only alleviate but also aggravate Tau aggregation and hence identification and analysis of chaperones that modulate Tau-aggregation and toxicity are required to understand biological and pathogenic mechanisms involved in Tauopathy, and (b) genetic or pharmacological manipulation of specific chaperone activities could be of possible therapeutic value for treating Tau-induced neurodegeneration.

We began this study by screening a collection of 64 *Drosophila* chaperones for their ability to modulate neurodegeneration caused by the expression of a pathogenic human Tau-protein variant $hTau^{V337M}$ in the *Drosophila* compound eye. We describe here a detailed analysis of Pfdn5, a subunit of the Prefoldin complex, which is shown to be involved in the proper folding of translationally derived actin and tubulin monomers [31, 32] in the regulation of neuronal microtubule stability and Tau-induced neurotoxicity *in vivo*. We report that Prefoldin 5 colocalizes with axonal microtubules and physically associates with stable microtubules. Loss of Pfdn5 resulted in a remarkable reduction in tubulin levels, disrupting

microtubules in otherwise wild-type *Drosophila*, as well as the aggregation of Tau in axons of the *Drosophila* hTau^{V337M} disease model. While Pfdn5 deletion exacerbates Tau-induced neurotoxicity, overexpression of Pfdn5 slows down the age-dependent progression of neurodegeneration and suppresses the learning and long-term memory deficits associated with Tau-induced neurotoxicity. These and other observations described in subsequent sections of this paper suggest that (1) In addition to its role as a cotranslational chaperone for tubulin, Pfdn5 has direct roles in the stability of mature microtubule filaments, and (2) Pfdn5 stabilizes microtubules, prevents neuronal loss and delays the onset of Tau-induced neurotoxicity. Since the overexpression of Pfdn5 restored the Tau-induced neurological abnormalities to the control levels without causing any detectable changes in synaptic morphology, cognitive impairment, or organismal health, we suggest that Pfdn5 could be a possible therapeutic target for Tauopathies.

RESULTS

A reverse-genetic screen of *Drosophila* chaperones identified Prefoldins as genetic modifiers of Tau-induced neurodegeneration

To identify chaperones that modulate Tau-induced neurodegeneration, we performed a screen for chaperones whose RNAi-based knockdown would modify progressive cytotoxicity observed in the eyes of *Drosophila* expressing human Tau^{V337M}. We used the hTau^{V337M} model because its expression in the eye resulted in moderate phenotypes, and therefore, allowed us to score for both enhancement or suppression of eye-ommatidial degeneration visibly [24, 33]. We coexpressed this transgenic construct (*UAS-hTau^{V337M}*) with each of 109 RNAi lines (targeting 64 chaperones) in the *Drosophila* eye using the pan-retinal driver *GMR-Gal4* and examined how each RNAi line influenced ommatidial degeneration in hTau^{V337M} expressing flies, seven days post-eclosion (Figure S1). We identified 20 chaperones that enhanced the

neurotoxicity and 15 that suppressed hTau^{V337M}-induced ommatidial degeneration (Figure 1 and Figure S1). Consistent with the previous studies [34, 35], we found that the knockdown of Hsp70 enhanced Tau-induced neurodegeneration (Figure S1I-I" and AH), validating the authenticity of this screen. In addition, the screen identified novel candidate Tau modulators. These notably included *Drosophila* orthologs of Prefoldins, tubulin binding cofactor E (TBCE) and chaperonin containing TCP1 (CCT), chaperones known to co-translationally regulate proper folding of tubulin or actin monomers (Figure 1C-L). Knockdown of Prefoldin subunits by different independent RNAi constructs strongly enhanced the ommatidial degeneration (Figure 1C-I). Similar effects were also seen following the knockdown of CCT or TBCE (Figure 1J-L).

The effect of Pfdn5 knockdown on Tau-induced eye degeneration, measured by quantifying the percentage of the degenerated eye area, was particularly robust compared to the hTau^{V337M} expressing flies (*GMR-Gal4>UAS-hTau^{V337M}*: 42.74 ± 1.59% vs *GMR-Gal4>UAS-hTau^{V337M}; UAS-Pfdn5 RNAi*: 85.06 ± 3.62%; $p < 0.001$) (Figure 1M), Moreover, prior cell culture studies have supported the idea that Prefoldin functions to regulate the solubility of aggregate-prone proteins [36, 37]. For instance, the deletion of Pfdn is accompanied by the accumulation of PolyQ or Htt aggregates in cell lines [38, 39]. In order to explore whether this proposed role of Prefoldin could be relevant to the control of Tau aggregation and neurodegeneration *in vivo*, and the finding that Pfdn5 get downregulated in Alzheimer's patients [40, 41], we selected Pfdn5 for careful and detailed analysis.

Prefoldin 5 regulates microtubule organization and levels of tubulin monomers

Pfdn5 is a component of the hetero-hexameric Prefoldin complex, which regulates the folding of nascent actin and tubulin monomers [32, 42]. To rigorously analyse the neuronal functions of Pfdn5, we generated loss-of-function mutants of Pfdn5 using CRISPR/Cas9-based genome editing. We created two independent *Pfdn5* mutants (Δ*Pfdn5^{15}* and Δ*Pfdn5^{40}*) using

two distinct pairs of gRNAs (Figure 2A). Both these *Pfdn5* mutants were null alleles, as no *Pfdn5* transcript was detected in the mutants (Figure S2A). Both homozygous and transheteroallelic mutants of Pfdn5 exhibited larval lethality at the L3 developmental stage (Figure 2A). These findings suggest that *Pfdn5* is an essential gene required ubiquitously for survival.

Analysis of third instar larval NMJ in *Pfdn5* mutants revealed the presence of several supernumerary boutons (Figure S2G-N). Prior work has shown that induction of supernumerary boutons can result from destabilizing the microtubule cytoskeleton at the NMJ [43, 44]. We therefore, investigated whether loss of Pfdn5 can influence axonal microtubules. We visualized microtubules using the monoclonal antibody 22C10, which labels the microtubule-associated protein Futsch in neurons. Futsch-positive loops are seen within a subset of stable presynaptic boutons [45]. Boutons containing such loops were greatly reduced in the *Pfdn5* mutant (control: 19.98 ± 2.18 vs $\Delta Pfdn5^{15/40}$: 7.72 ± 1.62; $p < 0.001$), and this reduction was restored to the control levels ($\Delta Pfdn5^{15/40}$: 7.72 ± 1.62 vs *Elav-Gal4/+; UAS-Pfdn5/+;* $\Delta Pfdn5^{15/40}$: 27.39 ± 2.21; $p < 0.001$) upon pan-neuronal expression of a *Pfdn5* transgene in *Pfdn5* mutant background (Figure 2B-F). Consistent with this, we found a significant reduction in the intensity of acetylated tubulin, which represents long-lived, stable microtubules, at the synapses and in the muscle of *Pfdn5* mutant compared to the control (synapses - control: 0.54 ± 0.04 vs. $\Delta Pfdn5^{15/40}$: 0.36 ± 0.03: $p <0.001$; muscles - control: 530.1 ± 71.56 vs. $\Delta Pfdn5^{15/40}$: 141.9 ± 8.43: $p < 0.001$) (Figure S3). The reduced acetylated tubulin intensity at *Pfdn5* null mutant synapses was restored by the pan-neuronal expression of *Pfdn5* transgene (Figure S3). Taken together, the data supports a function of Pfdn5 in regulating microtubule stability and organization *in vivo*.

Pfdn5 is also a known cotranslational chaperone for monomeric tubulin [46]. We therefore also examined whether and how loss of Pfdn5 altered levels of tubulin monomers.

Using RT-PCR, we found that the transcript level of tubulin was not altered in the *Pfdn5* mutants, suggesting that Pfdn5 does not alter tubulin gene transcription or transcript stability (Figure S3). In contrast, western blotting revealed about 85% reduction in the α-tubulin monomers (control: 1.00 ± 0.00 vs Δ*Pfdn5*$^{15/40}$: 0.11 ± 04; $p < 0.001$), about 70 percent reduction in β-tubulin (control: 1.00 ± 0.00 vs Δ*Pfdn5*$^{15/40}$: 0.31 ± 09 $p < 0.001$) and about 60% reduction in ace-tubulin levels (control: 1.00 ± 0.00 vs Δ*Pfdn5*$^{15/40}$: 0.46 ± 0.04; $p < 0.001$) in the *Pfdn5* mutant compared to the control (Figure 2G-J). These reductions were not seen when a *Pfdn5* transgene was ubiquitously expressed in *Pfdn5* mutant background (Figure 2G-J). The observation that β-actin levels remained unchanged in *Pfdn5* mutants is not particularly surprising, given a prior report indicating a differential requirement of the *Drosophila* Prefoldin complex in actin and tubulin biogenesis [47]. Together, these data are consistent with: a) *Drosophila* Pfdn5 serving as an evolutionarily conserved function in cotranslational folding of monomeric tubulin; and b) an additional role may be performed by Pfdn5 in the regulation of mature microtubule filaments in neurons. One or both of these functions could potentially be required for the stabilization of axonal microtubules.

Pfdn5 is a novel neuronal microtubule-associated protein

To assess the function of Pfdn5, we began by generating antisera against the full-length Pfdn5. Western blot analysis using Pfdn5 antibody revealed a protein band of ~18 kDa in the larval lysates that was absent in *Pfdn5* mutants, thus validating the specificity of the antibody (Figure S2B). In larval fillets examined by immunocytochemistry, anti-Pfdn5 staining was dramatically reduced in the mutant, with faint residual staining consistent with a low level of maternally provided Pfdn5 (Figure 3A-B''' and Figure S2C-F). The Pfdn5 staining was restored upon expression of the Pfdn5 transgene in the Pfdn5 mutant background (Figure 3B-C'''). Careful examination shows that Pfdn5 colocalized with axonal microtubule (labelled with α-tubulin antibody) in wild-type larvae (Figure 3A-A'''). The Pearson's correlation coefficient of

0.60 ± 0.02 across pixels labelled by α-Tubulin and Pfdn5 in axons further strengthens that a tight colocalization exists between Pfdn5 and neuronal microtubules (Figure 3D).

To further test whether Pfdn5 associates with microtubules, we stabilized microtubules using Taxol and performed a microtubule-binding experiment [48]. We found Pfdn5 in the pellet fraction when microtubules were stabilized with Taxol but not under the condition where the microtubules were severed using Nocodazole. The quantification revealed a substantially higher Pfdn5 binding to stabilized microtubules when compared to non-stabilized microtubule control (Taxol: 36.67 ± 7.56, vs control: 7.83 ± 2.92; $p < 0.001$) (Figure 3E-G). Consistent with our immunocytochemistry results, we found that Pfdn5 binds with the taxol-stabilised microtubule. This unexpected localization of Pfdn5 to neuronal microtubule filaments and its binding to the stable microtubule points to a role for this protein beyond its function as a cotranslational chaperone, potentially in the organization or the stability of axonal microtubule cytoskeleton.

Loss of Pfdn5 phenocopies and synergistically aggravates the Tau-induced synaptic defects

Since microtubules regulate morphological features of synapses [45] and loss of Pfdn5 resulted in reduced stable microtubules, we next asked if *Pfdn5* mutants show distinctly altered synaptic architecture at their NMJ. Both the homozygous and heteroallelic mutant combination showed numerous supernumerary boutons with altered synaptic morphology when compared to the control (control: 2.25 ± 0.41 vs. $\Delta Pfdn5^{15/40}$: 18.25 ± 1.27; $p < 0.001$) (Figure 4A-B and 4J). Increased supernumerary boutons in the *Pfdn5* mutant were completely restored upon pan-neuronal expression of a wild-type *Pfdn5* transgene using *Elav-Gal4* in the *Pfdn5* mutant background ($\Delta Pfdn5^{15/40}$: 18.25 ± 1.27 vs *Elav-Gal4/+; UAS-Pfdn5/+;* $\Delta Pfdn5^{15/40}$: 2.94 ± 0.67; $p < 0.001$) (Figure 4C and 4J) further confirming that these phenotypes were caused by *Pfdn5* mutations and not unknown potential background mutations. Expression of *Pfdn5* in

muscles using *mef2-Gal4* failed to rescue the lethality or the synaptic defects (Δ*Pfdn5*$^{15/40}$: 18.25 ± 1.27 vs *UAS-Pfdn5/+; mef2-Gal4,* Δ*Pfdn5*$^{15/40}$: 15.60 ± 0.86; $p > 0.75$) (Figure 4D and 4J) suggesting that synaptic phenotype arise due to loss of Pfdn5 in neurons and not muscles.

Ectopic satellite boutons and disrupted microtubules that we observed in *Pfdn5* mutant larval NMJs appeared very similar to those previously described in *Drosophila* expressing hTau^{V337M} in motor neurons [24, 44, 49]. This apparent similarity, together with our identification of Pfdn5 as a genetic modifier of hTau^{V337M}-induced cytotoxicity, led us to more closely examine phenotypic similarities between *Pfdn5* mutant and hTau^{V337M} expressing animals, as well as genetic interactions between *Pfdn5* and hTau^{V337M}. We first confirmed that the loss of Pfdn5 phenocopies the Tau^{V337M}-induced morphological defects at synapses (Figure 4E-F). We then tested the effects of loss and gain of Pfdn5 on Tau^{V337M} phenotypes.

Morphological NMJ phenotypes induced by expressing hTau^{V337M} pan-neuronally using *Elav-Gal4* were strongly enhanced in a *Pfdn5* mutant background (Figure 4G and 4I-K). While satellite bouton numbers in *Elav-Gal4/UAS-hTau*^{V337M} and Δ*Pfdn5*$^{15/40}$ were: 18.25 ± 1.27 and 14.06 ± 1.00 respectively, this was significantly increased in *Elav-Gal4/UAS-hTau*^{V337M}*;* Δ*Pfdn5*$^{15/40}$ combination (32.25 ± 3.22; $p < 0.001$) (Figure 4J). Subsequently, total bouton number was significantly increased in *Elav-Gal4/UAS-hTau*^{V337M}*;* Δ*Pfdn5*$^{15/40}$ combination animals (60.24 ± 3.76; $p < 0.001$) compared to either *Elav-Gal4/UAS-hTau*^{V337M} (36.00 ± 2.65) or Δ*Pfdn5*$^{15/40}$ (38.38 ± 2.15) alone. Similarly, bouton area (in μm^2) at NMJs of *Elav-Gal4/UAS-hTau*^{V337M}*;* Δ*Pfdn5*$^{15/40}$ combination animals (2.29 ± 0.20) were substantially smaller than either *Elav-Gal4/UAS-hTau*^{V337M} (6.40 ± 0.45) or Δ*Pfdn5*$^{15/40}$ (5.09 ± 0.28) alone (Figure 4K). Consistently expressing a more severe form of pathological Tau (hTau^{R406W}) in the *Pfdn5* mutation background also resulted in further enhancement in the synaptic phenotypes as well as the larval lethality (Figure S4). Thus, loss of Pfdn5 aggravates not only Tau-induced

eye degeneration (Figure 1) but also specific Tau-induced synaptic defects, suggestive of function in a common pathway.

Loss of Pfdn5 enhances pathological Tau aggregation in larval brain and axons

Tau induced neurotoxicity directly correlates with the extent of Tau phosphorylation and its deposition as insoluble aggregates [33, 50]. Hence, we performed additional experiments to explore mechanisms by which Pfdn5 levels could influence Tau function. We considered a model in which Pfdn5 acts to prevent Tau aggregation, thereby suppressing the Tau-induced neurodegeneration. The immunocytochemistry revealed that animals lacking Pfdn5 showed a remarkable increase in Tau-aggregates in the larval brain (Tau punctae with size > 3 μm^2 per brain lobe: *Elav-Gal4/UAS-hTau*^{V337M}: 1.13 ± 0.39 vs *Elav-Gal4/UAS-hTau*^{V337M}*;* Δ*Pfdn5*$^{15/40}$: 10.50 ± 2.57; $p < 0.001$) (Figure 5A-F). Consistent with these observations, hTau distribution in *Pfdn5* mutant axons revealed substantially higher number of hTau-aggregates compared to animals with normal levels of Pfdn5 (*Elav-Gal4/UAS-hTau*^{V337M}: 0.25 ± 0.09 /100 μm^2 vs *Elav-Gal4/UAS-hTau*^{V337M}*;* Δ*Pfdn5*$^{15/40}$: 2.9 ± 0.41 / 100 μm^2; $p < 0.001$) (Figure 5G-J" and 4K). The increased hTau punctae in *Pfdn5* mutants was significantly suppressed upon normalizing the level of Pfdn5 in neurons. Analysis of fluorescence intensity profiles across the Tau puncta showed a 4-fold increase in Tau intensity, further supporting that Tau indeed forms aggregates in the absence of Pfdn5 (Figure S5A-C). Additional experiments involving quantification of axonal hTau using immunofluorescence revealed that levels of Tau were significantly reduced in animals overexpressing hTau^{V337M} in *Pfdn5* mutants compared to animals expressing hTau^{V337M} alone (Figure 5G-J" and 5L). Similar results were obtained when the phospho-Tau antibody was used to assess Tau levels and aggregates (Figure S5D-F). These data reveal that Pfdn5 suppresses Tau aggregation in the brain and axons.

Together, (a) the marked increase of aggregated hTau in the absence of Pfdn5 and (b) enhancement of the Tau-associated phenotypes by loss of Pdfn5 indicate that, Pdfn5 prevents

the transition of hTau from soluble and/or microtube-associated state to an aggregated, insoluble and pathogenic state.

Neuronal overexpression of Pfdn5 or Pfdn6 ameliorates the hTau-induced age-dependent progression of the neurodegeneration.

The observations above indicate that loss of Pfdn5 enhances the neurotoxicity in the *Drosophila* Tauopathy model. We therefore, further tested whether overexpression of Pfdn5 could alleviate Tau-induced neurodegeneration. We examined the effects of Pfdn5/6 overexpression on hTau^{V337M} induced eye degeneration. *GMR-Gal4*-mediated overexpression of Pfdn5 or Pfdn6 in eyes significantly rescued hTau^{V337M}-induced ommatidial degeneration in 7-day-old flies (Figure 6A-D'). Previous reports suggest that Tau-induced eye degeneration exacerbates and worsens with age [51, 52]. Therefore, we examined the effect of the coexpression of Pfdn5 or Pfdn6 and hTau^{V337M} in 14 and 30-day-old flies (Figure 6E-J'). Consistent with prior reports, eye roughness and ommatidial degeneration worsened with age in hTau^{V337M} expressing flies. However, upon overexpression of Pfdn5 and Pfdn6, there was no progression of hTau^{V337M}-induced ommatidial degeneration with age (Figure 6K-L). We found that 30-day-old *UAS-hTau^{V337M}/+; GMR-Gal4/+* flies showed 29.12 ± 2.3% fused ommatidia and 70.96 ± 3.00% degenerated eye area. This eye degeneration was greatly suppressed when either Pfdn5 (% fused ommatidia, *UAS-hTau^{V337M}/+; GMR-Gal4/UAS-Pfdn5*: 2.98 ± 0.31; $p < 0.001$: % degenerated eye area, *UAS-hTau^{V337M}/+; GMR-Gal4/UAS-Pfdn5*: 5.30 ± 0.94; $p < 0.001$) or Pfdn6 (% fused ommatidia, *UAS-hTau^{V337M}/+; GMR-Gal4/UAS-Pfdn6*: 2.78 ± 0.60; $p < 0.001$: % degenerated eye area *UAS-hTau^{V337M}/+; GMR-Gal4/UAS-Pfdn6*: 3.83 ± 1.37; $p < 0.001$) was coexpressed with pathological hTau (Figure 6M-N). In order to ascertain that the suppression of eye degeneration was not due to the Gal4 dilution, we coexpressed the neutral gene product GFP along with hTau^{V337M}. As expected, we found no change in the Tau-induced eye phenotype when expressed alone or with GFP (Figure

S6A-D). These data suggest that the suppression of Tau-induced neurotoxicity was due to the expression of Pfdn5 or Pfdn6.

Overexpression of Pfdn5 suppressed not only hTau^{V337M}-induced neurotoxicity but also in a different Tauopathy model, hTau^{R406W}, which causes more severe neurotoxicity than hTau^{V337M} in the fly compound eye (degenerated eye area: *GMR-Gal4>UAS-hTau^{R406W}*: 82.15 ± 3.194 vs. *GMR-Gal4>UAS-hTau^{R406W}; UAS-Pfdn5*: 63.11 ± 3.49) (Figure S6E-G), indicating that Pfdn5 can mitigate the neurodegeneration caused by at least one another variant/structural conformations of hTau.

A key pathological feature of Tau-induced neurodegeneration is age-dependent vacuolization, a neuropathological feature directly indicative of neuronal death in the brain. Brain vacuolization is observed not only in human tauopathies but also in vertebrate and *Drosophila* models of Tauopathy [53]. We therefore tested whether elevating the expression level of Pfdn5 or Pfdn6 could mitigate the appearance of vacuoles that can be detected in the brains of 21-day-old flies expressing hTau [54]. We neuronally coexpressed hTau^{V337M} alone or together with Pfdn5 or Pfdn6 using *Elav-Gal4* and examined whole-mount brain preparations stained with rhodamine-phalloidin using confocal microscopy [55]. Consistent with the previous reports, we found several large vacuoles in the 21-day flies expressing hTau^{V337M}. The average number and size of the vacuoles in *Elav-Gal4/UAS-hTau^{V337M}* (35.67 ± 5.04 vacuoles/ brain, and 328.7 ± 82.24 μm average vacuole size) was far higher compared to the control *Elav-Gal4/+* (4.67 ± 1.45 vacuoles/ brain, and 9.27 ± 1.41 μm average vacuole size) (Figure 6O-P and 6S-T). Coexpression of Pfdn5 or Pfdn6 with hTau^{V337M} significantly reduced the number of vacuoles in *Elav-Gal4/UAS-hTau^{V337M}* flies. Indeed, vacuole numbers and size were restored to near control levels in *Elav-Gal4/UAS-hTau^{V337M}*; *UAS-Pfdn5/+* (3.75 ± 0.48 and 19.4 ± 4.42 μm) and *Elav-Gal4/UAS-hTau^{V337M}*; *UAS-Pfdn6/+* flies; (5.00 ± 1.47; 16.92 ± 0.89 μm) respectively (Figure 6Q-R and 6S-T). Altogether, these data indicate that

increased expression of Pfdn5 or Pfdn6 can remarkably counteract neuronal loss and delay the onset and progression of the neurodegenerative cascade induced in Tauopathy.

Expression of Pfdn5 or Pfdn6 suppresses Tau-induced memory impairment

Cognitive decline is a common preclinical and early feature of Tauopathies, seen well before substantial vacuolization in patient brains [56]. Hence, we further examined whether Pfdn5 or Pfdn6 overexpression could rescue cognitive and behavioral deficits caused by $hTau^{V337M}$ in the *Drosophila* brain. Because memory impairment is a known central condition in major Tauopathies (Orr et al., 2017), we tested the impact of $hTau^{V337M}$ expression on its own or in the presence of Pfdn5 or Pfdn6 for the ability of flies to form long-term associative memories. We used a recently developed method to assess long-term aversive olfactory conditioning memory [57], wherein bitter food ($CuSO_4$) serves as an unconditioned stimulus, which was paired with a conditioned stimulus, 2,3 butanedione (2,3 BD) over 8- cycles of training. Long-term memory was measured as an increased aversion towards the odorant 2,3 BD (measured in a Y-maze-based binary odor-choice assay) that persists 24 hours after 8-cycle training (Figure 7A). While untrained flies (naïve) showed a normal response to the odorant, the $CuSO_4$-trained flies (trained) showed proper memory performance towards the conditioned odorant. We found that the control flies (*UAS-hTau*^{V337M}/+) exhibit normal chemotactic responses towards odor and memory response against the conditioned odor in a Y-maze *(UAS-hTau*^{V337M}/+: naïve, 23.66 ± 2.42 v/s trained, 10.4 ± 2.14; $p < 0.001$) (Figure 7B). However, animals expressing $hTau^{V337M}$ in neurons *(Elav-Gal4/UAS-hTau*^{V337M}: naïve, 28.39 ± 3.47 v/s trained, 29.13 ± 4.65; $p = 0.90$) were memory deficient. They showed significantly reduced memory performance, as evidenced by their Preference Index being not different from the control flies of the same genotype (Figure 7C).

Next, we assessed whether the expression of Prefoldins impacted the memory deficit phenotype of flies expressing $hTau^{V337M}$. We first examined the effect of expression of Pfdn5

or Pfdn6 on memory performance. We found that pan-neuronal expression of either Pfdn5 (*Elav-Gal4/+; UAS-Pfdn5/+*: naïve, 18.27 ± 2.75 v/s trained, -4.43 ± 3.21; $p < 0.001$) or Pfdn6 (*Elav-Gal4/+; UAS-Pfdn6/+*: naïve, 18.37 ± 3.19 v/s trained, -0.88 ± 4.73; $p < 0.001$) does not cause any defect in naive odor response or memory performance after training (Figure 7D-E). However, coexpression of Pfdn5 significantly rescued the $hTau^{V337M}$-induced memory defects *(Elav-Gal4/UAS-$hTau^{V337M}$; UAS-Pfdn5/+*: naïve, 14.28 ± 1.96 v/s trained, -1.5 ± 1.7; $p < 0.001$) (Figure 7F). Similarly, co-expression of Pfdn6 also significantly restored the $hTau^{V337M}$-induced memory defects *(Elav-Gal4/UAS-$hTau^{V337M}$; UAS-Pfdn6/+*: naïve, 20.73 ± 4.58 v/s trained, -0.52 ± 5.07; $p < 0.001$) (Figure 7G). Together, these data strengthen our observations that neuronal expression of Pfdn5 or Pfdn6 not only rescues Tau-induced neurodegeneration but also learning and memory deficits.

Cotranslational functions of Pfdn5 do not completely explain its effects on neuronal microtubule stability, synapse morphology and Tau-aggregation

Consistent with cell culture and biochemical studies [46, 58], *Drosophila* Pfdn5 regulates tubulin monomers essential for microtubule assembly. Thus, one mechanism by which Pfdn5 influences Tau, could be via its effect on tubulin levels. However, since Pfdn5 colocalizes and binds neuronal microtubules, it could, alternatively, directly stabilize microtubules in axons and, by allowing Tau association with microtubules, prevent aggregation of free cytoplasmic Tau protein. To examine these models, we increased tubulin monomer levels in *Pfdn5* mutants by neuronally expressing *α-Tub* transgene and asked if it restored tubulin levels in the fly, and whether such restoration would be sufficient to rescue the neuronal microtubules and synaptic defects observed in *Pfdn5* mutants. Neuronal expression of *α-Tub* in *Pfdn5* mutant background restored both α- and β-tubulin monomers as well as ace-Tubulin to near wild-type levels (ace-Tubulin level: *$\Delta Pfdn5^{15/40}$* (0.34 ± 0.13) vs *Elav-Gal4>UAS-α-Tubulin; $\Delta Pfdn5^{15/40}$* (1.38 ± 0.15); $p < 0.01$) (Figure 8A and Figure S7A-D). However, this

was insufficient to rescue the axonal microtubule level and organization (Tubulin intensity at synapses: *ΔPfdn5*$^{15/40}$ (0.18 ± 0.01), *Elav-Gal4>UAS-α-Tubulin; ΔPfdn5*$^{15/40}$ (0.23 ± 0.01); p > 0.24) (Figure 8B-E) or synaptic phenotypes associated with *Pfdn5* mutations (satellite boutons: *ΔPfdn5*$^{15/40}$ (15.5 ± 1.48), *Elav-Gal4>UAS-α-Tubulin; ΔPfdn5*$^{15/40}$ (14.25 ± 1.39); p > 0.65) (Figure S7E-I). Moreover, axonal hTau aggregates seen in neuronally expressing hTau^{V337M} in Pfdn5 mutants were not reduced when tubulin monomer levels were restored (hTau punctae: *Elav-Gal4/UAS-hTau*^{V337M}*;* Δ*Pfdn5*$^{15/40}$: 3.32 ± 0.65 / 100 μm^2; vs *Elav-Gal4/UAS-hTau*^{V337M}*; UAS-α-tubulin,* Δ*Pfdn5*$^{15/40}$: 2.9 ± 0.57 / 100 μm^2; p > 0.80) (Figure 8F-I). Thus, the data suggest that in addition to its role as a cochaperone for tubulin monomers, Pfdn5 has an additional and potentially local role in stabilizing the neuronal microtubules as well as in preventing hTau aggregation.

DISCUSSION

Through varied and detailed analyses performed in established *Drosophila* Tauopathy models, we identify Prefoldin as a crucial component of chaperone systems that mitigate hTau-aggregation induced neurodegeneration. The experiments that lead to this conclusion provide three significant insights. First, that Prefoldin acts *in vivo* to suppress multiple measures of Tau-mediated degeneration. Second, that the mechanism of Prefoldin action in Tau-toxicity goes beyond its established role in co-translational folding of monomeric tubulin. Third, and finally, that overexpression of Prefoldin is sufficient to delay the progression of Tau-toxicity *in vivo*. We consider each of these issues in turn below.

Prefoldin acts *in vivo* to suppress multiple measures of Tau-mediated degeneration

Seminal work by others in the field has both established the value of modeling Tauopathies in *Drosophila* and described a series of independent Tau-induced degenerative

phenotypes displayed by these models [59-62]. The initial discovery that led to the rest of our current study was the identification of subunits of the prefoldin complex in a genetic screen for modifiers of Tau-toxicity. Knockdown of Pdfn components significantly enhanced eye-ommatidial degeneration in hTau^{V337M} expressing animals, suggestive of a role for this chaperone network in controlling the onset and progression of Tauopathies. Given the peripheral location of photoreceptors in the eye, it was important to more deeply assess the role of the identified chaperone components in the central nervous system. Such additional experiments confirmed that loss of Pfdn5 enhanced several additional hTau^{V337M}-induced phenotypes, including synaptic organization. In addition, loss of Pfdn5 resulted in a striking increase in large Tau protein aggregates in larval axons as well as in the larval brain. These data demonstrate an essential role for Pfdn in restricting hTau toxicity *in vivo*. However, more dramatic was the observation that neuronal overexpression of either Pfdn5 or Pfdn6 was sufficient to mitigate hTau-induced brain vacuolization and memory decline. Together, these observations demonstrate a pivotal role for Pfdn, or at least its Pfdn5 and Pfdn6 subunits, in suppressing Tau-pathologies.

Mechanism of Prefoldin action in Tau-toxicity

Molecular analysis of FTDP-17/ FTLD-tau mutations, as well as biochemical analysis of the pathogenic proteins, has shown that most disease-causing Tau mutations liberate Tau from microtubules and free the protein to form cytoplasmic aggregates [63-65]. Therefore, a simple potential mechanism by which Pfdn5 influences Tau toxicity could be through its effect on reducing levels of tubulin monomer, which would be predicted to reduce the availability of stable microtubules and thereby liberate excess Tau to form potentially pathogenic aggregates in the cytosol. Consistent with this, studies in mice and *C. elegans* have shown that neurons with reduced tubulin levels are highly susceptible to early onset of Tauopathies [66-68]. We noted that our screen for modulators of Tau-induced neurotoxicity also identified TBCE and

the components of the CCT complex, which represent additional players of a chaperone network known to participate in the cotranslational folding of nascent actin or tubulin monomers [69-71]. Further, our experiments showed that Pfdn5 mutations disrupt axonal microtubule organization as revealed by a reduction in the levels and organization of the microtubule-associated protein Futsch in axonal terminals of *Pfdn5* mutants (Figure 2) [72-74]. And finally, a prior observation that the Tau-induced eye degeneration is enhanced by the knockdown of TBCE, has been proposed to be caused by perturbed microtubule dynamics in both *Drosophila* models and human patients [26, 75, 76].

Despite the above observations, the effect on tubulin monomer levels does not completely explain how Pfdn influences microtubule organization or Tau toxicity. First, we report the unexpected but robust observation that Pdfn5 is a microtubule-associated protein, physically associated with stable axonal microtubules, and, therefore, well positioned to directly influence microtubule stability (Figure 3). Second and more directly, we find that genetic restoration of α-tubulin and β-tubulin monomer as well as acetylated tubulin levels, was not sufficient to rescue the synaptic defects observed in *Pfdn5* mutants (Figure 8). Thus, Pfdn5 appears to influence Tau toxicity through a mechanism downstream of its known roles in cotranslational folding of tubulin. While this could be via its function as a novel microtubule-associated protein, an additional possibility we consider is that Pfdn, and by extension other known cotranslational chaperones, could act additionally and directly as holdases or disaggregases for Tau and/or other aggregation-prone proteins. There is considerable circumstantial evidence to indicate posttranslational and direct roles for Prefoldin, as well as CCT, in preventing the aggregation of misfolded proteins. For instance, Prefoldin not only inhibits the formation of larger Htt aggregates [38] or amyloid β-aggregates [37] but also solubilizes the amyloid oligomers and inhibits their fibril formation under *in vitro* conditions [36, 37]. Similarly, CCT/ TRiC complex physically associates with the polyQ repeats of Htt

protein and remodels pathogenic aggregates *in vitro* [77, 78]. These evidence supports a direct role of Prefoldin and CCT as 'disaggregase' or 'aggregate remodellar' for aggregate-prone proteins and might regulate assembly/disassembly of Tau protein.

The identification of this cytoskeleton-regulatory chaperone network as a major modulator of Tauopathy supports the hypothesis that an age-dependent compromise in the chaperone activity could vitiate the onset and progression of multiple forms of Tauopathies and potentially other neurodegenerative diseases [79, 80]. Pfdn5 levels have been reported to decrease with age in a mouse model of Tauopathy [81]; our findings provide direct evidence that even a minimal amount of pathological hTau in the absence of Pfdn5 could induce the early onset of hTau-induced neurodegeneration. Moreover, our finding that neuronal expression of α-tubulin rescues the hTau-induced synaptic defects in a manner that critically requires Pfdn5 activity extends the functional requirement of Prefoldins in the suppression of Tauopathies beyond their reported activity in cell culture or *in vitro* models [37-39, 82]

Prefoldin overexpression as a strategy to mitigate Tauopathies

Our work suggests that stabilizing the components of this chaperone system, particularly Pfdn5 or Pfdn6, could be a promising therapeutic approach for delaying Tau-associated neuropathies. Neuronal overexpression of Pfdn5 or Pfdn6 did not result in any detectable changes in synaptic morphogenesis or age-dependent ommatidial degeneration. However, coexpression of Pfdn5 or Pfdn6 with the pathological variant of hTau remarkably suppressed Tau-induced synaptic defects, prevented brain vacuolization, and rescued memory defects (Figure 6 and Figure 7). This provides clear evidence that Pfdn5/Pfdn6-dependent microtubule regulation could potentially suppress Tau-induced neurodegeneration. These conclusions are supported by prior observations that expressing an acetylation mimic form of tubulin [49] or stabilizing microtubules [44] rescues the synaptic defects induced in the *Drosophila* Tauopathy model.

Do Prefoldins have a general neuroprotective role? In neuronal cell line, human Prefoldins colocalize with PolyQ-expanded protein Huntingtin and prevent the formation of toxic aggregates, supporting its role in the suppression of aggregation-induced neurotoxicity [38]. Moreover, recent compilation and analysis of proteomic data identified CCT components, TBCE as well as Prefoldin subunits, including PFDN5 that get downregulated in human Alzheimer's disease brain tissue [40, 41, 83-86]. In addition, whole blood mRNA expression data from Alzheimer's patients revealed downregulation of PFDN5 transcript [41]. These findings support crucial requirement of PFDN5 in suppressing multiple forms of neuropathies. Our data mechanistically extends these studies by revealing that Pfdn5 directly stabilizes neuronal microtubules, assists in proper partitioning of Tau onto the stable microtubules and suppresses the formation of pathological Tau aggregates. Importantly, our data reveal that expression of Pfdn5, whether ubiquitous or neuron-specific, does not induce any observable synaptic or microtubule-associated defects in neurons. This finding holds significant therapeutic promise since modulating Pfdn5 or Pfdn6 expression or stability could safely and effectively mitigate neurodegenerative diseases associated with microtubule instability, such as Tauopathies and possibly FUS-induced neurodegeneration [87].

CONCLUDING REMARKS

Based on our findings, we propose a model in which Pfdn5 regulates microtubule formation and stability by two non-exclusive mechanisms: a) by regulating the folding of nascent tubulin monomers and b) by directly associating and stabilizing microtubules in neurons (Figure 9). Both the functions of Pfdn5 are essential for regulating synaptic morphogenesis and Tau partitioning onto the microtubules. Normalizing the tubulin monomers to near wild-type levels was insufficient to rescue the axonal microtubule organization or suppress the Tau-aggregation in the absence of Pfdn5. This further supports the model that

Pfdn5-dependent tubulin stabilization is essential for Tau partitioning and that Tau aggregation is microtubule-dependent. Thus, while the conventional chaperone function of Prefoldins is essential for tubulin folding, direct association of Pfdn5 with stable microtubules to limit its turnover in neurons is crucial for suppressing Tau-aggregation. Further elucidation of the underlying mechanisms of Pfdn5-mediated neuroprotection and chemical screens to identify novel small molecules may pave the way for novel strategies to preserve neuronal function and combat neurodegeneration.

MATERIAL AND METHODS

Stocks and *Drosophila* husbandry

The *Drosophila* stocks were maintained at 25°C in standard cornmeal medium containing sucrose, agar, and yeast granules. The larvae for experiments were grown at 25°C in protein-rich media (80g/L cornflour, 40g/L dextrose, 20g/L sucrose, 18g/L agar, 15g/L yeast extract, 4% (v/v) propionic acid, 0.06% (v/v) ortho-phosphoric acid and 0.07% methyl-4-hydroxy benzoate/Tego) under non-crowded conditions. The w^{1118} was used as control unless otherwise stated. All the genetic combinations and recombination were made using standard *Drosophila* genetics. The crosses for RNAi-mediated knockdown and the rescue experiments were grown at 25°C. The following *Drosophila* lines were used in this study: *UAS-hTau*^{V337M} [54], *UAS-hTau*^{R406W} [54], *UAS-α-Tub84B* (BL-7373), *actin5C-Gal4* (BL-25374); *Elav*^{C155}*-Gal4* (BL-458); *mef2-Gal4* (BL-50742); and *GMR-Gal4* (BL-9146). Details of RNAi lines used in this study are mentioned in Supplemental Table 1.

Scanning electron microscopy

The flies were immersed in fixative (1% glutaraldehyde, 1% formaldehyde, and 1M sodium cacodylate, pH 7.2) for 2 hr, followed by subsequent washes and dehydration via an ethanol series. The samples were then dried and sputter-coated as previously described [88].

The flies were mounted on carbon conductive tabs stuck on aluminium stubs and imaged using a Zeiss scanning electron microscope (Carl Zeiss, Germany).

Generation of *Pfdn5* loss-of-function mutants and transgenes

To generate the loss-of-function mutants of Pfdn5, two sets of gRNAs were designed for the Pfdn5 genomic region using the CRISPR Optimal Target Finder online tool. The two gRNA pairs (gRNA1FP, gRNA1RP, and gRNA2FP, gRNA2RP) were cloned into a dual gRNA pCFD4 vector having a BbsI restriction site using Gibson Assembly Kit (New England Biolabs Ltd, UK) following the manufacturer's guidelines. The pCFD4 vector containing Pfdn5 gRNAs was injected into *Drosophila* embryos to generate the transgene. Next, the transgenic flies containing the Pfdn5 gRNAs were crossed with *nanos-Cas9* (BL-54591) to create the deletion of the *Pfdn5* gene in the germline cells. Following standard genetic crosses, lines were established in F2 generation, and *Pfdn5* deletion was screened by PCR using primers Pfdn5_FP1 and Pfdn5_RP. Two null mutants of Pfdn5, $\Delta Pfdn5^{15}$ (606 bp deletion), and $\Delta Pfdn5^{40}$ (577 bp deletion) were obtained and verified by sequencing using primer: Pfdn5_Seq FP.

To generate Pfdn5 or Pfdn6 transgenes, a full-length Pfdn5 or Pfdn6 ORF was amplified from cDNA and cloned in Gal4-based expression vector pUASt at EcoRI and NotI restriction sites. The pUASt vector containing the Pfdn5 or Pfdn6 ORF was injected into *Drosophila* embryos to generate the transgene. Semiquantitative RT-PCR was used to assess the expression of *Pfdn5* transcript in *Pfdn5* mutants. In brief, total RNA was isolated from larval fillets using TRIzol reagent (Invitrogen, Waltham, MA, USA). Reverse transcription was performed on 1 μg total RNA using Superscript™ II Reverse Transcriptase (Invitrogen, Waltham, MA, USA) using an oligo-dT primer to make cDNA. The resulting cDNA was used for PCR to analyze the level of *Pfdn5* transcript using primers Pfdn5_RTFP and Pfdn5_RTRP. The list of primers used in this study is reported in Supplemental Table 2.

Generation of Pfdn5 antibody

To generate antibodies against Pfdn5, the full-length Pfdn5 was amplified from cDNA using primers Pfdn5_pET28 FP and Pfdn5_pET RP and cloned in the pET-28a (+) bacterial expression vector at NotI and EcoRI restriction sites. The His-tagged fusion protein was expressed in BL21 codon+ cells, purified from inclusion bodies using the standard protein purification method from the pellet fraction, and injected into mice (animal facility, IISER Bhopal). The antibody was used at 1:200 dilution on fillets and 1:5000 dilution for western blotting.

Immunocytochemistry

Wandering third instar larvae were dissected on a sylgard plate in cold calcium-free HL3 and fixed in 4% paraformaldehyde in PBS for 30 minutes or in methanol for 5 minutes. The larval fillets were washed three times in PBS containing 0.2% Triton X-100, followed by blocking for one hour in 0.2% PBST containing 5% BSA. Fillets were fixed in the methanol for 5 mins to stain the ace-tubulin in the muscles. The fillets were incubated overnight at 4°C with a primary antibody followed by fluorophore-conjugated secondary antibodies at room temperature for 90 minutes. Finally, larval fillets were mounted on a glass slide with Fluoromount-G™ aqueous mounting medium (Thermofisher, Waltham, MA, USA). Primary antibodies used in the study, mouse anti-CSP (ab49, 1:50), mouse anti-Futsch (22C10, 1:50), and mouse anti-β-tubulin (E7, 1:50) were obtained from the Developmental Studies Hybridoma Bank (University of Iowa, USA). Other primary antibodies used in this study are mouse anti-dPfdn5 (this study, 1:200), mouse anti-ace-tubulin (1:500, Sigma-Aldrich, Missouri, USA), anti-Tau (T46, 1:100, Invitrogen, Waltham, MA, USA) and anti-phospho-Tau (AT8, 1:100, Invitrogen, Waltham, MA, USA). The fluorophore-conjugated secondary antibody Alexa Fluor 488 or Alexa Fluor 568 (Thermo Fisher Scientific, Waltham, MA, USA) was used at 1:800 dilution. Alexa Fluor 488 or Rhodamine conjugated anti-HRP (Jackson ImmunoResearch,

Baltimore, PA, USA) were used at 1:800 dilution. Hoechst (Thermo Fisher Scientific, Waltham, MA, USA) was used at 1:5000 dilution for 5 mins.

The brain staining for assessing vacuolization was done as previously described [55]. Briefly, the adult flies of appropriate genotypes were anesthetized and beheaded. The head was fixed in 4% PFA in 1X PBS containing 0.5% Triton X-100 for 20 min. The brain was dissected and fixed for another 2 hours, washed with PBST, and incubated with Hoechst (1:5000) and Alexa fluor 568 conjugated Phalloidin (1:100, Thermo Fisher Scientific, Waltham, MA, USA) cocktail in PBST for 24 hours. The brains were washed five times with PBST, followed by a final wash in 1X PBS for 30 minutes to remove the residual detergents or air sac, and mounted with Fluoromount-G™ aqueous mounting medium (Thermo Fisher Scientific, Waltham, MA, USA) on a glass slide for visualization.

Western blot analysis

Third instar larval body wall muscle or adult *Drosophila* heads were homogenized in 1X SDS lysis buffer (50 mM Tris-Cl, pH 6.8; 25 mM KCl; 2 mM EDTA; 0.3 M sucrose; 2% SDS), boiled, and centrifuged at 3000g. The protein concentration was quantified using bicinchoninic acid (BCA) Protein assay [89]. The homogenized sample was then combined with an equal volume of 2× Laemmli buffer (50 mM Tris-HCl, pH 6.8; 2% SDS; 2% β-Mercaptoethanol; 0.1% Bromophenol blue and 10% glycerol). Subsequently, 25 µg of protein was separated on a 12% SDS-PAGE gel and transferred to a Hybond-LFP PVDF membrane (GE Healthcare, Illinois, USA). The membrane was blocked in 5% skimmed milk in 1X Tris-buffered saline (TBS) with 0.2% Tween-20 (0.2% TBST) for 1 hour at room temperature and then incubated overnight with primary antibody. After washing with 0.2% TBST, the membrane was incubated with HRP-conjugated secondary antibody for 1 hour at room temperature. The primary antibodies used were: mouse anti-Pfdn5 (this study, 1:5000), rabbit anti-α-tubulin (1:3000, CST, Mumbai, India), mouse anti-β-tubulin (E7, 1:300, DSHB,

University of Iowa, USA), mouse anti-ace-tubulin (1:5000, Sigma-Aldrich, St. Louis, Missouri, USA), anti-Tau (T46, 1:1000, Invitrogen, Waltham, MA, USA), anti-phospho-Tau (AT8, 1:1000, Invitrogen, Waltham, MA, USA) and mouse anti-Ran (1:2000, BD Biosciences, New Jersey, USA). Signals were detected using the LI-COR Odyssey imaging system (LI-COR Biosciences, Lincoln, USA).

In vivo microtubule-binding assay

Microtubule binding assay was performed as described previously [48, 90]. Fifty heads from wild-type adult flies were collected and homogenized in 100 µl of Buffer-C+ (50 mM (HEPES); pH 7.1, 1.0 mM MgCl2, 1.0 mM EGTA, protease inhibitor cocktail (Roche, Basel, Switzerland), and phosphatase inhibitor cocktail in the presence of 20 µM Taxol or 40 µM Nocodazole diluted in dimethylsulfoxide (DMSO). Homogenized heads were centrifuged at 1,000× g for 10 minutes, and an aliquot of the supernatant was subjected to western blotting as the "input fraction". The remaining supernatant was layered onto a two-volume cushion of Buffer-C+ with 50% sucrose. After centrifugation at 100,000× g for 30 minutes, one-third of the supernatant containing soluble tubulin was collected from the top of the tube as the cytosol fraction, and the pellet containing microtubule polymers and proteins bound to microtubules was resuspended in 100 µl of SDS-Tris-Glycine sample buffer. Protein concentration in each fraction was measured using the BCA Protein Assay Kit. Equal amounts of protein were loaded onto each lane of Tris-Glycine gels and analyzed by western blotting using anti-Pfdn5 or anti-ace-tubulin antibodies.

Memory paradigm for aversive associative olfactory conditioning

To induce long-term aversive conditioning memory (LTM), flies were trained to associate an attractive odorant with bitter food, $CuSO_4$, as described previously [57]. 4–5-day-old adult flies were trained on 0.75% agar media containing 85 mM sucrose and 80 mM $CuSO_4$ (punishment media); the same media without $CuSO_4$ was used as control media. Flies of specific genotypes

were first starved in glass vials overnight containing 0.75% agar (starvation media) and then transferred to punishment media vials. For delivering the odor, a filter paper (1.5 cm x 2 cm), soaked in 100 µl of 5% 2,3 BD (2,3 butanedione, attractive odorant), was placed in a porous odor cup fitted at the top of the punishment or control vials. Starved flies were transferred into the punishment or control vials for 5 minutes, followed by 5 minutes of incubation in an empty test tube. This training cycle was repeated eight times for both the punishment and control group of flies. For checking 1-day memory retention, flies are starved for 6 hours after the 8-cycle conditioning step, followed by a 5-minute food pulse and again starvation for 18 hours. The flies were then tested (24 hrs after training) for their preference towards 2,3 BD in a binary odor choice assay paradigm using a Y-maze, and the Response Index (RI) of the control and trained flies was calculated as previously described [57].

Quantifications and statistical analysis

Images were captured with a laser scanning confocal microscope (FV3000; Olympus) using 40x 1.3 NA or 60x 1.42 NA objectives. The images were processed using ImageJ (National Institutes of Health, USA) or Adobe Photoshop software (Adobe Inc., USA). NMJs from muscle 4 at A2 hemisegment were captured using a 60× 1.42 NA objective to calculate the bouton number. CSP-positive boutons were counted manually. For bouton area quantification, NMJs from muscle 4 at A2 hemisegment were captured, and the area of five terminal boutons was calculated by drawing a free-hand sketch around CSP-positive boutons. The control and experimental fillets were processed similarly for fluorescence quantification, and the fluorescence images were captured under the same settings for every experimental set. For quantification of AT8 and T46 level in the larval axons, HRP-marked boundaries were defined for each axon. The fluorescence intensity of AT8 or T46 was calculated and normalized with HRP fluorescence. To quantify the Tau punctae in the axons, z-projections of confocal images of third-instar larval axons were captured. T46 and AT8 positive punctae were

manually counted and normalized with the area of respective axons. To quantify the Tau punctae in the larval brain, fluorescence threshold was set and analysed using ImageJ. Tau punctae greater than > 3 μm^2 were quantified**.** The maximum area of individual vacuoles was defined using the Wand tool in ImageJ software to quantify the vacuole size. Subsequently, the traced vacuoles were assigned and saved as regions of interest (ROIs). The selected ROIs were stacked and measured to quantify the size of the vacuoles [55]. The total number of boutons with Futsch positive loops was quantified manually using ImageJ [91]. The previously reported protocol was followed for quantitative evaluation of eye pigmentation score [92, 93]. Briefly, the pigmented area in the eyes was measured using ImageJ as previously reported and subtracted from the total eye area. More than 4 eyes were analyzed for each genotype.

Colocalization analysis was performed using the JACoP ImageJ plugin [94]. A line was drawn across the axons and plot profiles were drawn using the ImageJ function Plot Profile. The density of Western bands was quantified using ImageJ software. For multiple comparisons, one-way ANOVA followed by post hoc Tukey's test or Student's t-test was used. GraphPad Prism 8 (GraphPad Software Inc., California, USA) was used to plot all the graphs. Error bars in all the histograms represent $\pm$SEM. *$p < 0.05$, **$p < 0.01$, ***$p < 0.001$.

ACKNOWLEDGMENTS

We thank the Bloomington *Drosophila* Stock Center (BDSC) and Vienna *Drosophila* Resource Centre (VDRC) for the fly stocks, the Developmental Studies Hybridoma Bank (DSHB), the University of Iowa for monoclonal antibodies, and Varun Chaudhary, Baskar Bakthavachalu, Sunando Datta and Sankar Jha for their inputs on this manuscript. We acknowledge the animal facility and Debasis Nayak, IISER Bhopal, for his help in generating the Pfdn5 antibody.

DATA AVAILABILITY

All data are contained within the article.

CONFLICT OF INTEREST

The authors express no conflict of interest.

FUNDING

This work was supported by a research grant from the Science and Engineering Research Board (SERB Project No- EMR/2016/004718), the Government of India and intramural funds from IISER Bhopal to V.K. Anjali acknowledges fellowship support from the University Grants Commission, Government of India. MR acknowledges support from a Wellcome Trust-HRB-SFI Investigator grant, a Science Foundation Ireland Future Frontiers Programme grant, and an ANRF VAJRA grant from the Government of India.

FIGURE LEGENDS

Figure 1: Prefoldin cochaperones are genetic modifiers of Tau-induced neurodegeneration

(A-L) Bright-field images of 7-day old *Drosophila* eyes expressing (A) *hTau*^{V337M} (control), (B) *GMR-Gal4>UAS-hTau*^{V337M}*; UAS-GFP* (Gal4 dilution control), (C) *GMR-Gal4>UAS-hTau*^{V337M}*; UAS-Pfdn4 RNAi*, (D), (E), (F) *GMR-Gal4>UAS-hTau*^{V337M}*; UAS-Pfdn5 RNAi*, (G), (H), (I) *GMR-Gal4>UAS-hTau*^{V337M}*; UAS-Pfdn6 RNAi*, (J) *GMR-Gal4>UAS-hTau*^{V337M}*; UAS-TBCE RNAi*, (K) *GMR-Gal4>UAS-hTau*^{V337M}*; UAS-CCT5 RNAi*, (L) *GMR-Gal4>UAS-hTau*^{V337M}*; UAS-CCT7 RNAi*.

(M) Histogram showing the percentage of degenerated area in eyes of 7-day old flies of genotypes: *UAS-hTau*^{V337M}*/+; GMR-Gal4/+* (42.74 ± 1.59), *UAS-hTau*^{V337M}*/+; GMR-Gal4/UAS-GFP* (46.7 ± 1.79), *UAS-hTau*^{V337M}*/+; GMR-Gal4/UAS-Pfdn4 RNAi* (*BL77412;* 63.9 ± 2.95), *UAS-hTau*^{V337M}*/+; GMR-Gal4/UAS-Pfdn5 RNAi* (*BL67815;* 61.6 ± 3.6), *UAS-hTau*^{V337M}*/+; GMR-Gal4/UAS-Pfdn5 RNAi* (*KK100796;* 85.06 ± 3.01), *UAS-hTau*^{V337M}*/+; GMR-Gal4/UAS-Pfdn5 RNAi* (*GD29812;* 64.44 ± 4.91), *UAS-hTau*^{V337M}*/+; GMR-Gal4/UAS-Pfdn6 RNAi* (*BL65365;* 70.95 ± 4.17), *UAS-hTau*^{V337M}*/+; GMR-Gal4/+; UAS-Pfdn6 RNAi/+* (*GD34204;* 98.57 ± 0.4), *UAS-hTau*^{V337M}*/+; GMR-Gal4/UAS-Pfdn6 RNAi* (*KK101541;* 77.11 ± 2.96), *UAS-hTau*^{V337M}*/+; GMR-Gal4/+; UAS-TBCE RNAi/+* (*BL34537;* 62.01 ± 5.65), *UAS-hTau*^{V337M}*/+; GMR-Gal4/+; UAS-CCT5 RNAi/+* (*BL41818;* 64.36 ± 2.43), *UAS-hTau*^{V337M}*/+; GMR-Gal4/+; UAS-CCT7 RNAi/+* (*BL34931;* 61.67 ± 4.47). *p<0.05; ***p<0.001; ns, not significant.

Figure 2: Loss of Pfdn5 disrupts microtubule organisation

(A) Generation of a loss-of-function mutant of Pfdn5 using CRISPR/Cas9-based genome editing. Schematic representation of the Pfdn5 genomic organization showing exons (solid black boxes, 1-3) and introns (thin black lines). Two loss-of-function Pfdn5 mutants with 606

bp (line-15) or 577 bp (line-40) deletion were obtained. Both the mutant lines are third-instar larval lethal.

(B) Schematic representation of Futsch loop organization in muscle 4 of A2 hemisegment in wild-type or *Pfdn5* mutant. *Pfdn5* mutant shows diffused Fustch loop organization and reduced loops at the terminal boutons.

(C-E') Confocal images of NMJ synapses at muscle 4 of A2 hemisegment showing Futsch loops in (C-C') control, (D-D') *ΔPfdn5*$^{15/40}$, (E-E') *Elav-Gal4>UAS-Pfdn5;* Δ*Pfdn5*$^{15/40}$ double immunolabeled with neuronal membrane marker, HRP (green) and 22C10 antibody against microtubule-associated protein, Futsch (magenta). The scale bar in E' for (C-E') represents 10 µm.

(F) Histogram showing the percentage of Futsch positive loops from muscle 4 at A2 hemi segment in control (19.98 ± 2.18), *ΔPfdn5*$^{15/40}$ (7.72 ± 1.62), *Elav-Gal4/+; UAS-Pfdn5/+;* Δ*Pfdn5*$^{15/40}$ (27.39 ± 2.21). ***p<0.001.

(G) Western blot showing protein levels of α-Tubulin, β-Tubulin, ace-Tubulin and Actin in control, *ΔPfdn5*$^{15/15}$, *ΔPfdn5*$^{40/40}$, Δ*Pfdn*$^{15/40}$ and *actin5C-Gal4>UAS-Pfdn5;* Δ*Pfdn5*$^{15/40}$. Ran protein levels were used as an internal loading control.

(H) Histogram showing the percentage of ace-Tubulin normalized with Ran in control (1.00 ± 0.00), *ΔPfdn5*$^{15/15}$ (0.50 ± 0.05), Δ*Pfdn*$^{40/40}$ (0.49 ± 0.04), *ΔPfdn5*$^{15/40}$ (0.46 ± 0.04), *actin5C-Gal4/UAS-Pfdn5;* Δ*Pfdn5*$^{15/40}$ (1.05 ± 0.13). **p<0.01.

(I) Histogram showing percentage of α-Tubulin normalised with Ran in control (1.00 ± 0.00), *ΔPfdn5*$^{15/15}$ (0.27 ± 0.04), Δ*Pfdn*$^{40/40}$ (0.16 ± 0.02), *ΔPfdn5*$^{15/40}$ (0.11 ± 0.04), *actin5C-Gal4/UAS-Pfdn5;* Δ*Pfdn5*$^{15/40}$ (0.85 ± 0.07). ***p<0.001.

(J) Histogram showing percentage of β-Tubulin normalised with Ran in control (1.00 ± 0.00), *ΔPfdn5*$^{15/15}$ (0.52 ± 0.04), Δ*Pfdn*$^{40/40}$ (0.39 ± 0.04), *ΔPfdn5*$^{15/40}$ (0.30 ± 0.09), *actin5C-Gal4/UAS-Pfdn5;* Δ*Pfdn5*$^{15/40}$ (1.03 ± 0.11). **p<0.01.

Figure 3: Pfdn5 is a novel microtubule-binding protein

(A-C''') Confocal images of NMJ synapses at muscle 4 of A2 hemisegment triple-labeled for Pfdn5 (green), α-Tubulin (blue), and HRP (magenta) showing that Pfdn5 colocalizes with microtubule cytoskeleton in (A-A''') in the wild-type larval neuronal axons and in the tracheal tubes, (B-B''') *Pfdn5* mutants show dramatically reduced Pfdn5 and α-Tubulin levels, (C-C''') *actin5C-Gal4*-mediated rescue (*actin5C-Gal4>UAS-Pfdn5;* $\Delta Pfdn5^{15/40}$) significantly restored the level of Pfdn5 and α-Tubulin. Arrows represent Pfdn5 colocalization with microtubule loops, which are not detectable in the *Pfdn5* mutants. The scale bar in C''' (for A-C''') represents 10 µm.

(D) Pearson's correlation coefficient to quantify colocalization between Pfdn5 and axonal microtubule.

(E) Schematic representation of the microtubule-binding protocol. Head lysate from wild-type flies, treated with Taxol or Nocodazole, was subjected to ultracentrifugation. The 'soluble fraction' contains free tubulin whereas the 'insoluble pellet fraction' contains the stabilized microtubule along with microtubule-binding proteins, which can be detected by western blotting. The details of the protocol is described in the material and methods section.

(F) Microtubule binding assay with *Drosophila* head lysate in the presence of Taxol or Nocodazole (diluted in DMSO). T represents (Total fraction: input fraction), S represents (Supernatant: free tubulin), and P represents (Pellet fraction: stabilized microtubule). Immunoblot with antibodies against ace-Tubulin or Pfdn5 detected increased Pfdn5 in the pellet fraction in the presence of Taxol but not Nocodazole. The binding of Pfdn5 with stabilized microtubules was calculated as the percentage of Pfdn5 in the pellet fraction. Ran was used as the loading control.

(G) Histogram showing the percentage of the Pfdn5 in the pellet fraction of *in vivo* microtubule binding assay in the presence of DMSO (7.83 ± 2.92), Nocodazole (0.42 ± 0.1), or Taxol (36.67 ± 7.56).

Figure 4: Loss of Pfdn5 mimics and enhances Tau-induced synaptic defects

(A-H') Confocal images of NMJ synapses at muscle 4 of A2 hemisegment showing synaptic morphology in (A-A') control, (B-B') *ΔPfdn5*$^{15/40}$, (C-C') *Elav-Gal4>UAS-Pfdn5;* Δ*Pfdn5*$^{15/40}$, (D-D') *mef2-Gal4>UAS-Pfdn5;* Δ*Pfdn5*$^{15/40}$, (E-E') *Elav-Gal4/+* (Gal4 control), (F-F') *Elav-Gal4>UAS-hTau*^{V337M}, (G-G') *Elav-Gal4>hTau*^{V337M}*;* Δ*Pfdn5*$^{15/40}$, (H-H') *Elav-Gal4>hTau*^{V337M}*;UAS-Pfdn5;* Δ*Pfdn5*$^{15/40}$ double immunolabeled for HRP (green), and CSP (magenta). The scale bar in H for (A-H') represents 10 µm. Arrows point to clustered satellite boutons.

(I) Histogram showing total number of boutons from muscle 4 at A2 hemisegment in control (35.25 ± 1.8), *ΔPfdn5*$^{15/40}$ (38.38 ± 2.15), *Elav-Gal4>UAS-Pfdn5;* Δ*Pfdn5*$^{15/40}$ (31.94 ± 1.18), *mef2-Gal4>UAS-Pfdn5;* Δ*Pfdn5*$^{15/40}$ (38.40 ± 2.17), *Elav-Gal4/+* (28.13 ± 1.51), *Elav-Gal4>UAS-hTau*^{V337M} (36.00 ± 2.65), *Elav-Gal4>hTau*^{V337M}*;* Δ*Pfdn5*$^{15/40}$ (60.34 ± 3.76), *Elav-Gal4>hTau*^{V337M}*; UAS-Pfdn5;* Δ*Pfdn5*$^{15/40}$ (33.69 ± 1.76). ***p<0.001; ns, not significant.

(J) Histogram showing number of satellite boutons from muscle 4 at A2 hemisegment in control (2.25 ± 0.41), *ΔPfdn5*$^{15/40}$ (18.25 ± 1.28), *Elav-Gal4>UAS-Pfdn5;* Δ*Pfdn5*$^{15/40}$ (2.94 ± 0.67), *mef2-Gal4>UAS-Pfdn5;* Δ*Pfdn5*$^{15/40}$ (15.6 ± 0.86), *Elav-Gal4/+* (2.2 ± 0.38), *Elav-Gal4>UAS-hTau*^{V337M} (14.06 ± 1.00), *Elav-Gal4>hTau*^{V337M}*;* Δ*Pfdn5*$^{15/40}$ (32.25 ± 3.2), *Elav-Gal4>hTau*^{V337M}*;UAS-Pfdn5;* Δ*Pfdn5*$^{15/40}$ (4.0 ± 0.5). ***p<0.001; ns, not significant.

(K) Histogram showing bouton area from muscle 4 at A2 hemi segment in control (5.7 ± 0.29), *ΔPfdn5*$^{15/40}$ (5.1 ± 0.28), *Elav-Gal4>UAS-Pfdn5;* Δ*Pfdn5*$^{15/40}$ (5.6 ± 0.2), *mef2-Gal4>UAS-Pfdn5;* Δ*Pfdn5*$^{15/40}$ (5.8 ± 0.2), *Elav-Gal4/+* (5.2 ± 0.4), *Elav-Gal4>UAS-hTau*^{V337M} (6.4 ± 0.4),

Elav-Gal4>hTau^{V337M}*;* Δ*Pfdn5*$^{15/40}$ (2.3 ± 0.2), *Elav-Gal4>hTau*^{V337M}*;UAS-Pfdn5;* Δ*Pfdn5*$^{15/40}$ (6.3 ± 0.3). ***p<0.001; ns, not significant.

Figure 5: Loss of Pfdn5 induces formation of hTau^{V337M} aggregates in larval neurons

(A) Schematic representation of pathological hTau distribution in larval brain lobes and axons of the control (left half) or *Pfdn5* mutant (right half) animals.

(B-E') Confocal single section images of third instar larval brain in (B-B') *Elav-Gal4/+* (control), (C-C') *Elav-Gal4>UAS-hTau*^{V337M}, (D-D') *Elav-Gal4>UAS-hTau*^{V337M}*;* Δ*Pfdn5*$^{15/40}$, (E-E') *Elav-Gal4>UAS-hTau*^{V337M}*; UAS-Pfdn5;* Δ*Pfdn5*$^{15/40}$ double immunolabeled with neuronal membrane marker, HRP (magenta), and T46 antibody against hTau (green). The scale bar in E' for (B-E') represents 10 µm. Arrows in E and E' point to the hTau punctae/aggregates in the brain.

(F) Histogram showing the quantification of the number of hTau punctae (>3 µm^2) in *Elav-Gal4/UAS-hTau*^{V337M} (1.13 ± 0.39), *Elav-Gal4/UAS-hTau*^{V337M}*; ΔPfdn5*$^{15/40}$ (10.5 ± 2.57), and *Elav-Gal4/UAS-hTau*^{V337M}*; UAS-Pfdn5/+; ΔPfdn5*$^{15/40}$ (0.17 ± 0.17). ***p<0.001.

(G-J") Confocal single section images of third instar larval axons in (G-G") *Elav-Gal4/+* (control), (H-H") *Elav-Gal4>UAS-hTau*^{V337M}, (I-I") *Elav-Gal4>UAS-hTau*^{V337M}*;* Δ*Pfdn5*$^{15/40}$ (J-J") *Elav-Gal4>UAS-hTau*^{V337M}*; UAS-Pfdn5;* Δ*Pfdn5*$^{15/40}$ double immunolabeled for HRP (magenta), and T46 antibody against hTau (green). The scale bar in J" for (G-J") represents 10 µm. Arrows in I and I" point to the hTau^{V337M} aggregates in axons.

(K) Histogram showing the quantification of the number of hTau punctae normalized with HRP positive area in *Elav-Gal4/UAS-hTau*^{V337M} (0.25 ± 0.1), *Elav-Gal4/UAS-hTau*^{V337M}*; ΔPfdn5*$^{15/40}$ (2.96 ± 0.4), and *Elav-Gal4/UAS-hTau*^{V337M}*; UAS-Pfdn5/+; ΔPfdn5*$^{15/40}$ (0.29 ± 0.1). ***p<0.001.

(L) Histogram showing the intensity of total hTau normalized with HRP in *Elav-Gal4/UAS-hTau*^{V337M} (0.59 ± 0.02), *Elav-Gal4/UAS-hTau*^{V337M}*; ΔPfdn5*$^{15/40}$ (0.27 ± 0.02), and *Elav-Gal4/UAS-hTau*^{V337M}*; UAS-Pfdn5/+; ΔPfdn5*$^{15/40}$ (0.46 ± 0.4). ***p<0.001.

Figure 6: Over-expression of Pfdn5 or Pfdn6 suppresses age-dependent progression of hTau-induced neurodegeneration

(A-D) Bright-field images of 7 days old *Drosophila* eyes expressing (A) *GMR-Gal4/+* (control), (B) *GMR-Gal4>UAS-hTau*^{V337M}, (C) *GMR-Gal4>UAS-hTau*^{V337M}*; UAS-Pfdn5*, (D) *GMR-Gal4>UAS-hTau*^{V337M}*; UAS-Pfdn6*.

(A'-D') Scanning electron microscopic images of 7-day old *Drosophila* eyes expressing (A') *GMR-Gal4/+* (control), (B') *GMR-Gal4>UAS-hTau*^{V337M}, (C') *GMR-Gal4>UAS-hTau*^{V337M}*; UAS-Pfdn5*, (D') *GMR-Gal4>UAS-hTau*^{V337M}*; UAS-Pfdn6*.

(E-G) Bright field images of 14-day old *Drosophila* eyes expressing (E) *GMR-Gal4>UAS-hTau*^{V337M}, (F) *GMR-Gal4>UAS-hTau*^{V337M}*; UAS-Pfdn5*, (G) *GMR-Gal4>UAS-hTau*^{V337M}*; UAS-Pfdn6*.

(E'-G') Scanning electron microscopic images of 14-day old *Drosophila* eyes expressing (E') *GMR-Gal4>UAS-hTau*^{V337M}, (F') *GMR-Gal4>UAS-hTau*^{V337M}*; UAS-Pfdn5*, (G') *GMR-Gal4>UAS-hTau*^{V337M}*; UAS-Pfdn6*.

(H-J) Bright field images of 30-day old *Drosophila* eyes expressing (H) *GMR-Gal4>UAS-hTau*^{V337M}, (I) *GMR-Gal4>UAS-hTau*^{V337M}*; UAS-Pfdn5*, (J) *GMR-Gal4>UAS-hTau*^{V337M}*; UAS-Pfdn6*.

(H'-J') Scanning electron microscopic images of 30-day old *Drosophila* eyes expressing (H') *GMR-Gal4>UAS-hTau*^{V337M}, (I') *GMR-Gal4>UAS-hTau*^{V337M}*; UAS-Pfdn5*, (J') *GMR-Gal4>UAS-hTau*^{V337M}*; UAS-Pfdn6*. The scale bar in J' for (A-J') represents 100 µm.

(K-L) Graph showing quantifications of age-dependent progression of ommatidial fusion (K) and percentage of degenerated eye area (L) in *GMR-Gal4>UAS-hTau*^{V337M}, *GMR-Gal4>UAS-*

hTau^{V337M}; UAS-Pfdn5 and *GMR-Gal4>UAS-hTau^{V337M}; UAS-Pfdn6*. Note that expression of Pfdn5 or Pfdn6 suppresses the Tau-induced neuronal death.

(M) Histogram showing the percentage of fused ommatidia in 30 days old flies in *GMR-Gal4/+* (0.00 ± 0.00), *UAS-hTau^{V337M}/+; GMR-Gal4/+* (29.12 ± 2.37), *UAS-hTau^{V337M}/+; GMR-Gal4/UAS-Pfdn5* (2.98 ± 0.31), *UAS-hTau^{V337M}/+; GMR-Gal4/UAS-Pfdn6* (2.78 ± 0.60). ***p<0.001.

(N) Histogram showing percentage of degenerated area in 30 days old flies in *GMR-Gal4/+* (0.00 ± 0.00), *UAS-hTau^{V337M}/+; GMR-Gal4/+* (70.96 ± 3.00), *UAS-hTau^{V337M}/+; GMR-Gal4/UAS-Pfdn5* (5.30 ± 0.94), *UAS-hTau^{V337M}/+; GMR-Gal4/UAS-Pfdn6* (3.83 ± 1.37). ***p<0.001.

(O-R) Confocal images of a single section of 21-day old adult brain in (O) *Elav-Gal4/+* (control), (P) *Elav-Gal4>UAS-hTau^{V337M}*, (Q) *Elav-Gal4>hTau^{V337M}; UAS-Pfdn5*, (R) *Elav-Gal4>hTau^{V337M}; UAS-Pfdn6* double immunolabeled with Hoechst (cyan), and Phalloidin (magenta). The insets represent the 3X magnified portion of the image. Arrows in the figure P inset point to the pathological vacuolar structures. The scale bar in R for (O-R) represents 10 µm.

(S) Histogram showing the quantification of number of vacuoles in 21 days old adult brain in *GMR-Gal4/+* (4.67 ± 1.45), *UAS-hTau^{V337M}/+; GMR-Gal4/+* (35.67 ± 5.04), *UAS-hTau^{V337M}/+; GMR-Gal4/UAS-Pfdn5* (3.75 ± 0.48), *UAS-hTau^{V337M}/+; GMR-Gal4/UAS-Pfdn6* (5.00 ± 1.47). ***p<0.001.

(T) Histogram showing the quantification of vacuole size (in µm^2) in 21-day old adult brain in *GMR-Gal4/+* (9.27 ± 1.41), *UAS-hTau^{V337M}/+; GMR-Gal4/+* (328.7 ± 82.24), *UAS-hTau^{V337M}/+; GMR-Gal4/UAS-Pfdn5* (19.4 ± 4.2), *UAS-hTau^{V337M}/+; GMR-Gal4/UAS-Pfdn6* (16.92 ± 0.89). **p<0.01.

Figure 7: Over-expression of Pfdn5 or Pfdn6 rescues Tau-induced defects in learning and memory

(A) Cartoon of Y-maze assay used for behavioural testing of conditioned odor preferences. Schematics of the protocol used to induce and measure a form of learning and memory [57]. During training, flies are exposed to a normally attractive odorant 2,3-butanedione (10^{-3}-fold dilution) in a spaced training protocol: 8X repeats of a training trial involving 5 minutes in the presence unpleasant medium (80 mM $CuSO_4$ + 85 mM sucrose and 0.75% agar) followed by 5 min in an air-filled empty vial. Trained flies were tested in a binary odor-choice assay in a Y-maze apparatus for their odor vs. air preference. Control flies were trained in 0.75 % agar media with 85 mM sucrose and similarly tested in Y-maze.

(B-G) Histogram showing the quantification of odor preference index of naïve and trained flies towards 2,3-BD in Y-maze showing normal memory in control. A reduction in the preference index after training reflects levels of learning and memory **(B)** *UAS-hTau^{V337M}/+*; naïve flies (23.66 ± 2.42), trained flies (10.4 ± 2.14), whereas pan-neuronal expression of the pathological variant hTau causes a defect in long-term memory response **(C)** *Elav-Gal4/UAS-hTau^{V337M}*; naïve flies (28.39 ± 3.47), trained flies (29.13 ± 4.65). Notably, pan-neuronal overexpression of Pfdn5 **(D)** *Elav-Gal4/+; UAS-Pfdn5/+*; naïve flies (18.27 ± 2.75), trained flies (-4.43 ± 3.21), pan-neuronal overexpression of Pfdn6 **(E)** *Elav-Gal4/+; UAS-Pfdn6/+*; naïve flies (18.37 ± 3.19), trained flies (-0.88 ± 4.73) were normal. Interestingly, pan-neuronal over-expression of Pfdn5 along with hTau^{V337M} expression rescues the learning and memory deficits in **(F)** *Elav-Gal4/UAS-hTau^{V337M}; UAS-Pfdn5/+*; naïve flies (14.28 ± 1.96), trained flies (-1.5 ± 1.7). Consistently, pan-neuronal over-expression of Pfdn6 along with hTau^{V337M} expression also rescues the learning and memory deficits in **(G)** *Elav-Gal4/UAS-hTau^{V337M}; UAS-Pfdn6/+*; naïve flies (20.73 ± 4.58), trained flies (-0.52 ± 5.07). n = 8 biological replicates in

each case. Error bars represent the standard error of the mean (SEM). **p < 0.01; ***p<0.001; ns, not significant.

Figure 8: Microtubule stability and Tau-association with microtubules require Pfdn5-functions downstream of tubulin monomer expression

(A) Western blot showing protein levels of ace-Tubulin, α-Tubulin, and β-Tubulin in control, Δ*Pfdn*$^{15/40}$, and *Elav-Gal4>UAS-α-Tubulin; ΔPfdn5*$^{15/40}$. Ran protein levels were used as an internal loading control.

(B-D') Confocal images of NMJ synapses showing synaptic microtubules in (B-B') control, (C-C') *ΔPfdn5*$^{15/40}$, (D-D') *Elav-Gal4>UAS-α-Tubulin; ΔPfdn5*$^{15/40}$ double immunolabeled for ace-Tubulin (magenta) and HRP (green). The scale bar in D' for (A-D') represents 10 µm. Arrows in C and D shows disrupted microtubules.

(E) Histogram showing ace-Tubulin intensity at the NMJ in control (0.47 ± 0.03), *ΔPfdn5*$^{15/40}$ (0.18 ± 0.01), *Elav-Gal4>UAS-α-Tubulin; ΔPfdn5*$^{15/40}$ (0.23 ± 0.01). ***p<0.001; ns, not significant.

(F-H') Confocal images of third instar larval axons in (F-F') *Elav-Gal4>UAS-hTau*^{V337M}, (G-G') *Elav-Gal4>UAS-hTau*^{V337M}*;* Δ*Pfdn5*$^{15/40}$, and (H-H') *Elav-Gal4>UAS-hTau*^{V337M}*; UAS-α-Tubulin,* Δ*Pfdn5*$^{15/40}$ double immunolabeled with neuronal membrane marker, HRP (green), and T46 antibody against total human Tau (magenta). The scale bar in H' for (F-H') represents 10 µm. Arrows point to the Tau-aggregates.

(I) Histogram showing the quantification of the number of Tau punctae per 100 µm^2 normalized with HRP positive area in *Elav-Gal4/UAS-hTau*^{V337M} (0.18 ± 0.05), *Elav-Gal4/UAS-hTau*^{V337M}*; ΔPfdn5*$^{15/40}$ (3.32 ± 0.65), and *Elav-Gal4>UAS-hTau*^{V337M}*; UAS-α-Tubulin,* Δ*Pfdn5*$^{15/40}$ (2.9 ± 0.57). ***p<0.001; **p<0.01.

Figure 9: A model depicting novel functional requirement of Pfdn5 in microtubule stabilization and its role in suppressing age-dependent neuropathy.

In axons, Pfdn5 physically associates with microtubules and stabilizes them, thereby suppressing the turnover of microtubules. The pathological Tau dislodges from microtubules in an age-dependent manner and forms pathological aggregates that induce neuronal death (Middle panel). Loss of Pfdn5 disrupts neuronal microtubules, resulting in abnormal synaptic morphogenesis and facilitating dislodging of microtubule-associated Tau, resulting in Tau-aggregates formation and stepping up the early onset of Tauopathies. An age-dependent reduction in the Pfdn5 levels or mutations in Pfdn5 could result in microtubule fragmentation and may facilitate Tau-induced neurotoxicity (Left panel). Pfdn5 suppresses Tau-aggregation in a manner that involves microtubule stability and does not appear to regulate Tau solubility directly. Notably, neuronal overexpression of Pfdn5 suppresses the microtubule disruption even in aged flies, thereby inhibiting the progression of Tauopathy (Right panel).

REFERENCES

1. Ross CA, Poirier MA. Protein aggregation and neurodegenerative disease. Nat Med. 2004;10 Suppl:S10-7. doi: 10.1038/nm1066. PubMed PMID: 15272267.
2. Soto C, Pritzkow S. Protein misfolding, aggregation, and conformational strains in neurodegenerative diseases. Nat Neurosci. 2018;21(10):1332-40. Epub 20180924. doi: 10.1038/s41593-018-0235-9. PubMed PMID: 30250260; PubMed Central PMCID: PMCPMC6432913.
3. Sweeney P, Park H, Baumann M, Dunlop J, Frydman J, Kopito R, et al. Protein misfolding in neurodegenerative diseases: implications and strategies. Transl Neurodegener. 2017;6:6. Epub 20170313. doi: 10.1186/s40035-017-0077-5. PubMed PMID: 28293421; PubMed Central PMCID: PMCPMC5348787.
4. Lashuel HA. Rethinking protein aggregation and drug discovery in neurodegenerative diseases: Why we need to embrace complexity? Curr Opin Chem Biol. 2021;64:67-75. Epub 20210623. doi: 10.1016/j.cbpa.2021.05.006. PubMed PMID: 34174698.
5. Iqbal K, Liu F, Gong CX, Grundke-Iqbal I. Tau in Alzheimer disease and related tauopathies. Curr Alzheimer Res. 2010;7(8):656-64. doi: 10.2174/156720510793611592. PubMed PMID: 20678074; PubMed Central PMCID: PMCPMC3090074.
6. Jouanne M, Rault S, Voisin-Chiret AS. Tau protein aggregation in Alzheimer's disease: An attractive target for the development of novel therapeutic agents. Eur J Med Chem. 2017;139:153-67. Epub 20170729. doi: 10.1016/j.ejmech.2017.07.070. PubMed PMID: 28800454.
7. Pinzi L, Bisi N, Sorbi C, Franchini S, Tonali N, Rastelli G. Insights into the Structural Conformations of the Tau Protein in Different Aggregation Status. Molecules. 2023;28(11). Epub 20230604. doi: 10.3390/molecules28114544. PubMed PMID: 37299020; PubMed Central PMCID: PMCPMC10254443.
8. Khanna MR, Kovalevich J, Lee VM, Trojanowski JQ, Brunden KR. Therapeutic strategies for the treatment of tauopathies: Hopes and challenges. Alzheimers Dement. 2016;12(10):1051-65. doi: 10.1016/j.jalz.2016.06.006. PubMed PMID: 27751442; PubMed Central PMCID: PMCPMC5116305.
9. Avila J, Lucas JJ, Perez M, Hernandez F. Role of tau protein in both physiological and pathological conditions. Physiol Rev. 2004;84(2):361-84. doi: 10.1152/physrev.00024.2003. PubMed PMID: 15044677.
10. Kent SA, Spires-Jones TL, Durrant CS. The physiological roles of tau and Abeta: implications for Alzheimer's disease pathology and therapeutics. Acta Neuropathol. 2020;140(4):417-47. Epub 20200729. doi: 10.1007/s00401-020-02196-w. PubMed PMID: 32728795; PubMed Central PMCID: PMCPMC7498448.
11. Robbins M, Clayton E, Kaminski Schierle GS. Synaptic tau: A pathological or physiological phenomenon? Acta Neuropathol Commun. 2021;9(1):149. Epub 20210909. doi: 10.1186/s40478-021-01246-y. PubMed PMID: 34503576; PubMed Central PMCID: PMCPMC8428049.
12. Wolfe MS. Tau mutations in neurodegenerative diseases. J Biol Chem. 2009;284(10):6021-5. Epub 20081022. doi: 10.1074/jbc.R800013200. PubMed PMID: 18948254.
13. Goedert M, Jakes R. Mutations causing neurodegenerative tauopathies. Biochim Biophys Acta. 2005;1739(2-3):240-50. doi: 10.1016/j.bbadis.2004.08.007. PubMed PMID: 15615642.
14. Tzioras M, McGeachan RI, Durrant CS, Spires-Jones TL. Synaptic degeneration in Alzheimer disease. Nat Rev Neurol. 2023;19(1):19-38. Epub 20221213. doi: 10.1038/s41582-022-00749-z. PubMed PMID: 36513730.
15. Guo W, Stoklund Dittlau K, Van Den Bosch L. Axonal transport defects and neurodegeneration: Molecular mechanisms and therapeutic implications. Semin Cell Dev Biol.

2020;99:133-50. Epub 20190918. doi: 10.1016/j.semcdb.2019.07.010. PubMed PMID: 31542222.
16. Stubbs K, Batchelor B, Sivanantharajah L, Sealey M, Ramirez-Moreno M, Ruiz E, et al. Tau-mediated axonal degeneration is prevented by activation of the Wld(S) pathway. Brain Commun. 2023;5(2):fcad052. Epub 20230309. doi: 10.1093/braincomms/fcad052. PubMed PMID: 37013175; PubMed Central PMCID: PMCPMC10066515.
17. Brunden KR, Zhang B, Carroll J, Yao Y, Potuzak JS, Hogan AM, et al. Epothilone D improves microtubule density, axonal integrity, and cognition in a transgenic mouse model of tauopathy. J Neurosci. 2010;30(41):13861-6. doi: 10.1523/JNEUROSCI.3059-10.2010. PubMed PMID: 20943926; PubMed Central PMCID: PMCPMC2958430.
18. Zhang B, Maiti A, Shively S, Lakhani F, McDonald-Jones G, Bruce J, et al. Microtubule-binding drugs offset tau sequestration by stabilizing microtubules and reversing fast axonal transport deficits in a tauopathy model. Proc Natl Acad Sci U S A. 2005;102(1):227-31. Epub 20041222. doi: 10.1073/pnas.0406361102. PubMed PMID: 15615853; PubMed Central PMCID: PMCPMC544048.
19. Yu TW, Lane HY, Lin CH. Novel Therapeutic Approaches for Alzheimer's Disease: An Updated Review. Int J Mol Sci. 2021;22(15). Epub 20210730. doi: 10.3390/ijms22158208. PubMed PMID: 34360973; PubMed Central PMCID: PMCPMC8348485.
20. Ostapchenko VG, Beraldo FH, Mohammad AH, Xie YF, Hirata PH, Magalhaes AC, et al. The prion protein ligand, stress-inducible phosphoprotein 1, regulates amyloid-beta oligomer toxicity. J Neurosci. 2013;33(42):16552-64. doi: 10.1523/JNEUROSCI.3214-13.2013. PubMed PMID: 24133259; PubMed Central PMCID: PMCPMC6618518.
21. Perez N, Sugar J, Charya S, Johnson G, Merril C, Bierer L, et al. Increased synthesis and accumulation of heat shock 70 proteins in Alzheimer's disease. Brain Res Mol Brain Res. 1991;11(3-4):249-54. doi: 10.1016/0169-328x(91)90033-t. PubMed PMID: 1661822.
22. Renkawek K, Bosman GJ, de Jong WW. Expression of small heat-shock protein hsp 27 in reactive gliosis in Alzheimer disease and other types of dementia. Acta Neuropathol. 1994;87(5):511-9. doi: 10.1007/BF00294178. PubMed PMID: 8059604.
23. Darling AL, Dahrendorff J, Creodore SG, Dickey CA, Blair LJ, Uversky VN. Small heat shock protein 22 kDa can modulate the aggregation and liquid-liquid phase separation behavior of tau. Protein Sci. 2021;30(7):1350-9. Epub 20210315. doi: 10.1002/pro.4060. PubMed PMID: 33686711; PubMed Central PMCID: PMCPMC8197419.
24. Blard O, Feuillette S, Bou J, Chaumette B, Frebourg T, Campion D, et al. Cytoskeleton proteins are modulators of mutant tau-induced neurodegeneration in Drosophila. Hum Mol Genet. 2007;16(5):555-66. Epub 20070219. doi: 10.1093/hmg/ddm011. PubMed PMID: 17309878.
25. Buchner J. Molecular chaperones and protein quality control: an introduction to the JBC Reviews thematic series. J Biol Chem. 2019;294(6):2074-5. Epub 20190109. doi: 10.1074/jbc.REV118.006739. PubMed PMID: 30626733; PubMed Central PMCID: PMCPMC6369298.
26. Dou F, Netzer WJ, Tanemura K, Li F, Hartl FU, Takashima A, et al. Chaperones increase association of tau protein with microtubules. Proc Natl Acad Sci U S A. 2003;100(2):721-6. Epub 20030109. doi: 10.1073/pnas.242720499. PubMed PMID: 12522269; PubMed Central PMCID: PMCPMC141063.
27. Warrick JM, Chan HY, Gray-Board GL, Chai Y, Paulson HL, Bonini NM. Suppression of polyglutamine-mediated neurodegeneration in Drosophila by the molecular chaperone HSP70. Nat Genet. 1999;23(4):425-8. doi: 10.1038/70532. PubMed PMID: 10581028.
28. Bhattacharya K, Weidenauer L, Luengo TM, Pieters EC, Echeverria PC, Bernasconi L, et al. The Hsp70-Hsp90 co-chaperone Hop/Stip1 shifts the proteostatic balance from folding towards degradation. Nat Commun. 2020;11(1):5975. Epub 20201125. doi: 10.1038/s41467-020-19783-w. PubMed PMID: 33239621; PubMed Central PMCID: PMCPMC7688965.

29. Criado-Marrero M, Gebru NT, Blazier DM, Gould LA, Baker JD, Beaulieu-Abdelahad D, et al. Hsp90 co-chaperones, FKBP52 and Aha1, promote tau pathogenesis in aged wild-type mice. Acta Neuropathol Commun. 2021;9(1):65. Epub 20210408. doi: 10.1186/s40478-021-01159-w. PubMed PMID: 33832539; PubMed Central PMCID: PMCPMC8033733.
30. Shelton LB, Baker JD, Zheng D, Sullivan LE, Solanki PK, Webster JM, et al. Hsp90 activator Aha1 drives production of pathological tau aggregates. Proc Natl Acad Sci U S A. 2017;114(36):9707-12. Epub 20170821. doi: 10.1073/pnas.1707039114. PubMed PMID: 28827321; PubMed Central PMCID: PMCPMC5594679.
31. Geissler S, Siegers K, Schiebel E. A novel protein complex promoting formation of functional alpha- and gamma-tubulin. EMBO J. 1998;17(4):952-66. doi: 10.1093/emboj/17.4.952. PubMed PMID: 9463374; PubMed Central PMCID: PMCPMC1170445.
32. Vainberg IE, Lewis SA, Rommelaere H, Ampe C, Vandekerckhove J, Klein HL, et al. Prefoldin, a chaperone that delivers unfolded proteins to cytosolic chaperonin. Cell. 1998;93(5):863-73. doi: 10.1016/s0092-8674(00)81446-4. PubMed PMID: 9630229.
33. Chau KW, Chan WY, Shaw PC, Chan HY. Biochemical investigation of Tau protein phosphorylation status and its solubility properties in Drosophila. Biochem Biophys Res Commun. 2006;346(1):150-9. Epub 20060530. doi: 10.1016/j.bbrc.2006.05.112. PubMed PMID: 16759647.
34. Kundel F, De S, Flagmeier P, Horrocks MH, Kjaergaard M, Shammas SL, et al. Hsp70 Inhibits the Nucleation and Elongation of Tau and Sequesters Tau Aggregates with High Affinity. ACS Chem Biol. 2018;13(3):636-46. Epub 20180117. doi: 10.1021/acschembio.7b01039. PubMed PMID: 29300447; PubMed Central PMCID: PMCPMC6374916.
35. Petrucelli L, Dickson D, Kehoe K, Taylor J, Snyder H, Grover A, et al. CHIP and Hsp70 regulate tau ubiquitination, degradation and aggregation. Hum Mol Genet. 2004;13(7):703-14. Epub 20040212. doi: 10.1093/hmg/ddh083. PubMed PMID: 14962978.
36. Sakono M, Zako T, Ueda H, Yohda M, Maeda M. Formation of highly toxic soluble amyloid beta oligomers by the molecular chaperone prefoldin. FEBS J. 2008;275(23):5982-93. doi: 10.1111/j.1742-4658.2008.06727.x. PubMed PMID: 19021772.
37. Sorgjerd KM, Zako T, Sakono M, Stirling PC, Leroux MR, Saito T, et al. Human prefoldin inhibits amyloid-beta (Abeta) fibrillation and contributes to formation of nontoxic Abeta aggregates. Biochemistry. 2013;52(20):3532-42. Epub 20130508. doi: 10.1021/bi301705c. PubMed PMID: 23614719.
38. Tashiro E, Zako T, Muto H, Itoo Y, Sorgjerd K, Terada N, et al. Prefoldin protects neuronal cells from polyglutamine toxicity by preventing aggregation formation. J Biol Chem. 2013;288(27):19958-72. Epub 20130517. doi: 10.1074/jbc.M113.477984. PubMed PMID: 23720755; PubMed Central PMCID: PMCPMC3707696.
39. Takano M, Tashiro E, Kitamura A, Maita H, Iguchi-Ariga SM, Kinjo M, et al. Prefoldin prevents aggregation of alpha-synuclein. Brain Res. 2014;1542:186-94. PubMed PMID: 24511594.
40. Askenazi M, Kavanagh T, Pires G, Ueberheide B, Wisniewski T, Drummond E. Compilation of reported protein changes in the brain in Alzheimer's disease. Nat Commun. 2023;14(1):4466. Epub 20230725. doi: 10.1038/s41467-023-40208-x. PubMed PMID: 37491476; PubMed Central PMCID: PMCPMC10368642.
41. Ji W, An K, Wang C, Wang S. Bioinformatics analysis of diagnostic biomarkers for Alzheimer's disease in peripheral blood based on sex differences and support vector machine algorithm. Hereditas. 2022;159(1):38. Epub 20221004. doi: 10.1186/s41065-022-00252-x. PubMed PMID: 36195955; PubMed Central PMCID: PMCPMC9531459.
42. Leroux MR, Fandrich M, Klunker D, Siegers K, Lupas AN, Brown JR, et al. MtGimC, a novel archaeal chaperone related to the eukaryotic chaperonin cofactor GimC/prefoldin. EMBO J. 1999;18(23):6730-43. doi: 10.1093/emboj/18.23.6730. PubMed PMID: 10581246; PubMed Central PMCID: PMCPMC1171735.

43. Saunders HAJ, Johnson-Schlitz DM, Jenkins BV, Volkert PJ, Yang SZ, Wildonger J. Acetylated alpha-tubulin K394 regulates microtubule stability to shape the growth of axon terminals. Curr Biol. 2022;32(3):614-30 e5. Epub 20220125. doi: 10.1016/j.cub.2021.12.012. PubMed PMID: 35081332; PubMed Central PMCID: PMCPMC8843987.
44. Xiong Y, Zhao K, Wu J, Xu Z, Jin S, Zhang YQ. HDAC6 mutations rescue human tau-induced microtubule defects in Drosophila. Proc Natl Acad Sci U S A. 2013;110(12):4604-9. Epub 20130304. doi: 10.1073/pnas.1207586110. PubMed PMID: 23487739; PubMed Central PMCID: PMCPMC3606981.
45. Roos J, Hummel T, Ng N, Klämbt C, Davis GW. Futsch regulates synaptic microtubule organization and is necessary for synaptic growth. Neuron. 2000;26(2):371-82. doi: Doi 10.1016/S0896-6273(00)81170-8. PubMed PMID: WOS:000087296500014.
46. Gestaut D, Zhao Y, Park J, Ma B, Leitner A, Collier M, et al. Structural visualization of the tubulin folding pathway directed by human chaperonin TRiC/CCT. Cell. 2022;185(25):4770-87 e20. doi: 10.1016/j.cell.2022.11.014. PubMed PMID: 36493755; PubMed Central PMCID: PMCPMC9735246.
47. Delgehyr N, Wieland U, Rangone H, Pinson X, Mao G, Dzhindzhev NS, et al. Drosophila Mgr, a Prefoldin subunit cooperating with von Hippel Lindau to regulate tubulin stability. Proc Natl Acad Sci U S A. 2012;109(15):5729-34. Epub 20120326. doi: 10.1073/pnas.1108537109. PubMed PMID: 22451918; PubMed Central PMCID: PMCPMC3326472.
48. Ando K, Maruko-Otake A, Ohtake Y, Hayashishita M, Sekiya M, Iijima KM. Stabilization of Microtubule-Unbound Tau via Tau Phosphorylation at Ser262/356 by Par-1/MARK Contributes to Augmentation of AD-Related Phosphorylation and Abeta42-Induced Tau Toxicity. PLoS Genet. 2016;12(3):e1005917. Epub 20160329. doi: 10.1371/journal.pgen.1005917. PubMed PMID: 27023670; PubMed Central PMCID: PMCPMC4811436.
49. Mao CX, Wen X, Jin S, Zhang YQ. Increased acetylation of microtubules rescues human tau-induced microtubule defects and neuromuscular junction abnormalities in Drosophila. Dis Model Mech. 2017;10(10):1245-52. Epub 20170817. doi: 10.1242/dmm.028316. PubMed PMID: 28819043; PubMed Central PMCID: PMCPMC5665452.
50. Aquino Nunez W, Combs B, Gamblin TC, Ackley BD. Age-dependent accumulation of tau aggregation in Caenorhabditis elegans. Front Aging. 2022;3:928574. Epub 20220819. doi: 10.3389/fragi.2022.928574. PubMed PMID: 36062211; PubMed Central PMCID: PMCPMC9437221.
51. Lacomme M, Hales SC, Brown TW, Stevanovic K, Jolicoeur C, Cai J, et al. Numb regulates Tau levels and prevents neurodegeneration in tauopathy mouse models. Sci Adv. 2022;8(42):eabm4295. Epub 20221019. doi: 10.1126/sciadv.abm4295. PubMed PMID: 36260685; PubMed Central PMCID: PMCPMC9581485.
52. Ishihara T, Hong M, Zhang B, Nakagawa Y, Lee MK, Trojanowski JQ, et al. Age-dependent emergence and progression of a tauopathy in transgenic mice overexpressing the shortest human tau isoform. Neuron. 1999;24(3):751-62. doi: 10.1016/s0896-6273(00)81127-7. PubMed PMID: 10595524.
53. Byrns CN, Saikumar J, Bonini NM. Glial AP1 is activated with aging and accelerated by traumatic brain injury. Nat Aging. 2021;1(7):585-97. Epub 20210708. doi: 10.1038/s43587-021-00072-0. PubMed PMID: 34723199; PubMed Central PMCID: PMCPMC8553014.
54. Wittmann CW, Wszolek MF, Shulman JM, Salvaterra PM, Lewis J, Hutton M, et al. Tauopathy in Drosophila: neurodegeneration without neurofibrillary tangles. Science. 2001;293(5530):711-4. Epub 20010614. doi: 10.1126/science.1062382. PubMed PMID: 11408621.
55. Behnke JA, Ye C, Moberg KH, Zheng JQ. A protocol to detect neurodegeneration in Drosophila melanogaster whole-brain mounts using advanced microscopy. STAR Protoc. 2021;2(3):100689. Epub 20210728. doi: 10.1016/j.xpro.2021.100689. PubMed PMID: 34382016; PubMed Central PMCID: PMCPMC8339312.

56. Hanseeuw BJ, Betensky RA, Jacobs HIL, Schultz AP, Sepulcre J, Becker JA, et al. Association of Amyloid and Tau With Cognition in Preclinical Alzheimer Disease: A Longitudinal Study. JAMA Neurol. 2019;76(8):915-24. doi: 10.1001/jamaneurol.2019.1424. PubMed PMID: 31157827; PubMed Central PMCID: PMCPMC6547132.
57. Mohandasan R, Thakare M, Sunke S, Iqbal FM, Sridharan M, Das G. Enhanced olfactory memory detection in trap-design Y-mazes allows the study of imperceptible memory traces in Drosophila. Learn Mem. 2022;29(10):355-66. Epub 20220930. doi: 10.1101/lm.053545.121. PubMed PMID: 36180129; PubMed Central PMCID: PMCPMC9536757.
58. Tahmaz I, Shahmoradi Ghahe S, Topf U. Prefoldin Function in Cellular Protein Homeostasis and Human Diseases. Front Cell Dev Biol. 2021;9:816214. Epub 20220117. doi: 10.3389/fcell.2021.816214. PubMed PMID: 35111762; PubMed Central PMCID: PMCPMC8801880.
59. Zhou L, McInnes J, Wierda K, Holt M, Herrmann AG, Jackson RJ, et al. Tau association with synaptic vesicles causes presynaptic dysfunction. Nat Commun. 2017;8:15295. Epub 20170511. doi: 10.1038/ncomms15295. PubMed PMID: 28492240; PubMed Central PMCID: PMCPMC5437271.
60. Vourkou E, Rouiz Ortega ED, Mahajan S, Mudher A, Skoulakis EMC. Human Tau Aggregates Are Permissive to Protein Synthesis-Dependent Memory in Drosophila Tauopathy Models. J Neurosci. 2023;43(16):2988-3006. Epub 20230303. doi: 10.1523/JNEUROSCI.1374-22.2023. PubMed PMID: 36868851; PubMed Central PMCID: PMCPMC10124960.
61. Bukhari H, Nithianandam V, Battaglia RA, Cicalo A, Sarkar S, Comjean A, et al. Transcriptional programs mediating neuronal toxicity and altered glial-neuronal signaling in a Drosophila knock-in tauopathy model. Genome Res. 2024;34(4):590-605. Epub 20240515. doi: 10.1101/gr.278576.123. PubMed PMID: 38599684; PubMed Central PMCID: PMCPMC11146598.
62. Shulman JM, Imboywa S, Giagtzoglou N, Powers MP, Hu Y, Devenport D, et al. Functional screening in Drosophila identifies Alzheimer's disease susceptibility genes and implicates Tau-mediated mechanisms. Hum Mol Genet. 2014;23(4):870-7. Epub 20130925. doi: 10.1093/hmg/ddt478. PubMed PMID: 24067533; PubMed Central PMCID: PMCPMC3900103.
63. Hong M, Zhukareva V, Vogelsberg-Ragaglia V, Wszolek Z, Reed L, Miller BI, et al. Mutation-specific functional impairments in distinct tau isoforms of hereditary FTDP-17. Science. 1998;282(5395):1914-7. doi: 10.1126/science.282.5395.1914. PubMed PMID: 9836646.
64. Dayanandan R, Van Slegtenhorst M, Mack TG, Ko L, Yen SH, Leroy K, et al. Mutations in tau reduce its microtubule binding properties in intact cells and affect its phosphorylation. FEBS Lett. 1999;446(2-3):228-32. doi: 10.1016/s0014-5793(99)00222-7. PubMed PMID: 10100846.
65. Guo T, Noble W, Hanger DP. Roles of tau protein in health and disease. Acta Neuropathol. 2017;133(5):665-704. Epub 20170406. doi: 10.1007/s00401-017-1707-9. PubMed PMID: 28386764; PubMed Central PMCID: PMCPMC5390006.
66. Miyasaka T, Shinzaki Y, Yoshimura S, Yoshina S, Kage-Nakadai E, Mitani S, et al. Imbalanced Expression of Tau and Tubulin Induces Neuronal Dysfunction in C. elegans Models of Tauopathy. Front Neurosci. 2018;12:415. Epub 20180620. doi: 10.3389/fnins.2018.00415. PubMed PMID: 29973863; PubMed Central PMCID: PMCPMC6019497.
67. Tatebayashi Y, Miyasaka T, Chui DH, Akagi T, Mishima K, Iwasaki K, et al. Tau filament formation and associative memory deficit in aged mice expressing mutant (R406W) human tau. Proc Natl Acad Sci U S A. 2002;99(21):13896-901. Epub 20021004. doi: 10.1073/pnas.202205599. PubMed PMID: 12368474; PubMed Central PMCID: PMCPMC129794.

68. Yoshiyama Y, Higuchi M, Zhang B, Huang SM, Iwata N, Saido TC, et al. Synapse loss and microglial activation precede tangles in a P301S tauopathy mouse model. Neuron. 2007;53(3):337-51. doi: 10.1016/j.neuron.2007.01.010. PubMed PMID: 17270732.
69. Serna M, Carranza G, Martin-Benito J, Janowski R, Canals A, Coll M, et al. The structure of the complex between alpha-tubulin, TBCE and TBCB reveals a tubulin dimer dissociation mechanism. J Cell Sci. 2015;128(9):1824-34. Epub 20150423. doi: 10.1242/jcs.167387. PubMed PMID: 25908846.
70. Gil-Krzewska AJ, Farber E, Buttner EA, Hunter CP. Regulators of the actin cytoskeleton mediate lethality in a Caenorhabditis elegans dhc-1 mutant. Mol Biol Cell. 2010;21(15):2707-20. Epub 20100616. doi: 10.1091/mbc.E09-07-0593. PubMed PMID: 20554764; PubMed Central PMCID: PMCPMC2912356.
71. Hansen WJ, Cowan NJ, Welch WJ. Prefoldin-nascent chain complexes in the folding of cytoskeletal proteins. J Cell Biol. 1999;145(2):265-77. doi: 10.1083/jcb.145.2.265. PubMed PMID: 10209023; PubMed Central PMCID: PMCPMC2133115.
72. Jin S, Pan L, Liu Z, Wang Q, Xu Z, Zhang YQ. Drosophila Tubulin-specific chaperone E functions at neuromuscular synapses and is required for microtubule network formation. Development. 2009;136(9):1571-81. Epub 20090318. doi: 10.1242/dev.029983. PubMed PMID: 19297412.
73. Roos J, Hummel T, Ng N, Klambt C, Davis GW. Drosophila Futsch regulates synaptic microtubule organization and is necessary for synaptic growth. Neuron. 2000;26(2):371-82. doi: 10.1016/s0896-6273(00)81170-8. PubMed PMID: 10839356.
74. Sherwood NT, Sun Q, Xue M, Zhang B, Zinn K. Drosophila spastin regulates synaptic microtubule networks and is required for normal motor function. PLoS Biol. 2004;2(12):e429. Epub 20041130. doi: 10.1371/journal.pbio.0020429. PubMed PMID: 15562320; PubMed Central PMCID: PMCPMC532392.
75. Battini R, Milone R, Aiello C, Astrea G, Sferra A, Pasquariello R, et al. Broadening the spectrum phenotype of TBCE-related neuron neurodegeneration. Brain Dev. 2021;43(9):939-44. Epub 20210613. doi: 10.1016/j.braindev.2021.05.015. PubMed PMID: 34134906.
76. Fujiwara H, Watanabe S, Iwata M, Ueda S, Nobuhara M, Wada-Kakuda S, et al. Inhibition of microtubule assembly competent tubulin synthesis leads to accumulation of phosphorylated tau in neuronal cell bodies. Biochem Biophys Res Commun. 2020;521(3):779-85. Epub 20191105. doi: 10.1016/j.bbrc.2019.10.191. PubMed PMID: 31699369.
77. Darrow MC, Sergeeva OA, Isas JM, Galaz-Montoya JG, King JA, Langen R, et al. Structural Mechanisms of Mutant Huntingtin Aggregation Suppression by the Synthetic Chaperonin-like CCT5 Complex Explained by Cryoelectron Tomography. J Biol Chem. 2015;290(28):17451-61. Epub 20150520. doi: 10.1074/jbc.M115.655373. PubMed PMID: 25995452; PubMed Central PMCID: PMCPMC4498080.
78. Tam S, Geller R, Spiess C, Frydman J. The chaperonin TRiC controls polyglutamine aggregation and toxicity through subunit-specific interactions. Nat Cell Biol. 2006;8(10):1155-62. Epub 20060917. doi: 10.1038/ncb1477. PubMed PMID: 16980959; PubMed Central PMCID: PMCPMC2829982.
79. Tittelmeier J, Nachman E, Nussbaum-Krammer C. Molecular Chaperones: A Double-Edged Sword in Neurodegenerative Diseases. Front Aging Neurosci. 2020;12:581374. Epub 20201006. doi: 10.3389/fnagi.2020.581374. PubMed PMID: 33132902; PubMed Central PMCID: PMCPMC7572858.
80. Cyske Z, Gaffke L, Pierzynowska K, Wegrzyn G. Tubulin Cytoskeleton in Neurodegenerative Diseases-not Only Primary Tubulinopathies. Cell Mol Neurobiol. 2023;43(5):1867-84. Epub 20221109. doi: 10.1007/s10571-022-01304-6. PubMed PMID: 36352320; PubMed Central PMCID: PMCPMC10287795.
81. Kadoyama K, Matsuura K, Takano M, Maekura K, Inoue Y, Matsuyama S. Changes in the expression of prefoldin subunit 5 depending on synaptic plasticity in the mouse hippocampus.

Neurosci Lett. 2019;712:134484. Epub 20190907. doi: 10.1016/j.neulet.2019.134484. PubMed PMID: 31505240.
82. Millan-Zambrano G, Rodriguez-Gil A, Penate X, de Miguel-Jimenez L, Morillo-Huesca M, Krogan N, et al. The prefoldin complex regulates chromatin dynamics during transcription elongation. PLoS Genet. 2013;9(9):e1003776. Epub 20130919. doi: 10.1371/journal.pgen.1003776. PubMed PMID: 24068951; PubMed Central PMCID: PMCPMC3777993.
83. Tao Y, Han Y, Yu L, Wang Q, Leng SX, Zhang H. The Predicted Key Molecules, Functions, and Pathways That Bridge Mild Cognitive Impairment (MCI) and Alzheimer's Disease (AD). Front Neurol. 2020;11:233. Epub 20200403. doi: 10.3389/fneur.2020.00233. PubMed PMID: 32308643; PubMed Central PMCID: PMCPMC7145962.
84. Leitner D, Pires G, Kavanagh T, Kanshin E, Askenazi M, Ueberheide B, et al. Similar brain proteomic signatures in Alzheimer's disease and epilepsy. Acta Neuropathol. 2024;147(1):27. Epub 20240130. doi: 10.1007/s00401-024-02683-4. PubMed PMID: 38289539; PubMed Central PMCID: PMCPMC10827928.
85. Sun Z, Kwon JS, Ren Y, Chen S, Walker CK, Lu X, et al. Modeling late-onset Alzheimer's disease neuropathology via direct neuronal reprogramming. Science. 2024;385(6708):adl2992. Epub 20240802. doi: 10.1126/science.adl2992. PubMed PMID: 39088624.
86. Hsieh YC, Guo C, Yalamanchili HK, Abreha M, Al-Ouran R, Li Y, et al. Tau-Mediated Disruption of the Spliceosome Triggers Cryptic RNA Splicing and Neurodegeneration in Alzheimer's Disease. Cell Rep. 2019;29(2):301-16 e10. doi: 10.1016/j.celrep.2019.08.104. PubMed PMID: 31597093; PubMed Central PMCID: PMCPMC6919331.
87. Kandhavivorn W, Glass H, Herrmannsdorfer T, Bockers TM, Uhlarz M, Gronemann J, et al. Restoring Axonal Organelle Motility and Regeneration in Cultured FUS-ALS Motoneurons through Magnetic Field Stimulation Suggests an Alternative Therapeutic Approach. Cells. 2023;12(11). Epub 20230529. doi: 10.3390/cells12111502. PubMed PMID: 37296623; PubMed Central PMCID: PMCPMC10252208.
88. Choudhury SD, Mushtaq Z, Reddy-Alla S, Balakrishnan SS, Thakur RS, Krishnan KS, et al. sigma2-Adaptin Facilitates Basal Synaptic Transmission and Is Required for Regenerating Endo-Exo Cycling Pool Under High-Frequency Nerve Stimulation in Drosophila. Genetics. 2016;203(1):369-85. Epub 20160226. doi: 10.1534/genetics.115.183863. PubMed PMID: 26920756; PubMed Central PMCID: PMCPMC4858786.
89. Simpson RJ. Quantifying protein by bicinchoninic Acid. CSH Protoc. 2008;2008:pdb prot4722. Epub 20080801. doi: 10.1101/pdb.prot4722. PubMed PMID: 21356880.
90. Feuillette S, Miguel L, Frebourg T, Campion D, Lecourtois M. Drosophila models of human tauopathies indicate that Tau protein toxicity in vivo is mediated by soluble cytosolic phosphorylated forms of the protein. J Neurochem. 2010;113(4):895-903. Epub 20100227. doi: 10.1111/j.1471-4159.2010.06663.x. PubMed PMID: 20193038.
91. Coyne AN, Siddegowda BB, Estes PS, Johannesmeyer J, Kovalik T, Daniel SG, et al. Futsch/MAP1B mRNA is a translational target of TDP-43 and is neuroprotective in a Drosophila model of amyotrophic lateral sclerosis. J Neurosci. 2014;34(48):15962-74. doi: 10.1523/JNEUROSCI.2526-14.2014. PubMed PMID: 25429138; PubMed Central PMCID: PMCPMC4244467.
92. Saitoh Y, Fujikake N, Okamoto Y, Popiel HA, Hatanaka Y, Ueyama M, et al. p62 plays a protective role in the autophagic degradation of polyglutamine protein oligomers in polyglutamine disease model flies. J Biol Chem. 2015;290(3):1442-53. Epub 20141205. doi: 10.1074/jbc.M114.590281. PubMed PMID: 25480790; PubMed Central PMCID: PMCPMC4340391.
93. Fujino Y, Ueyama M, Ishiguro T, Ozawa D, Ito H, Sugiki T, et al. FUS regulates RAN translation through modulating the G-quadruplex structure of GGGGCC repeat RNA in C9orf72-

linked ALS/FTD. Elife. 2023;12. Epub 20230718. doi: 10.7554/eLife.84338. PubMed PMID: 37461319; PubMed Central PMCID: PMCPMC10393046.
94. Bolte S, Cordelieres FP. A guided tour into subcellular colocalization analysis in light microscopy. J Microsc. 2006;224(Pt 3):213-32. doi: 10.1111/j.1365-2818.2006.01706.x. PubMed PMID: 17210054.

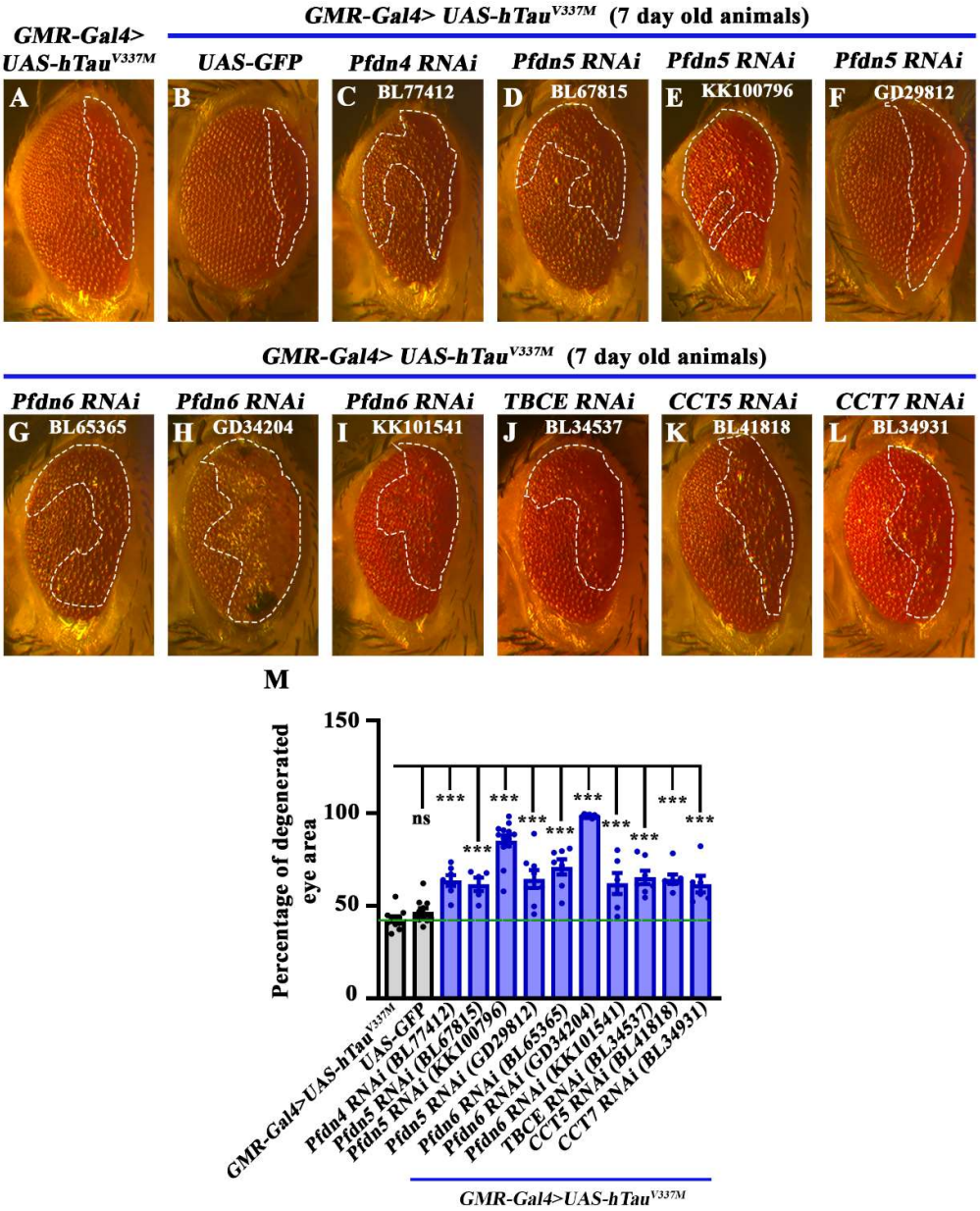
GMR-Gal4> UAS-hTau^{V337M} (7 day old animals)
GMR-Gal4> UAS-hTau^{V337M}
UAS-GFP
Pfdn4 RNAi
Pfdn5 RNAi
Pfdn5 RNAi
Pfdn5 RNAi
A
B
C BL77412
D BL67815
E KK100796
F GD29812
GMR-Gal4> UAS-hTau^{V337M} (7 day old animals)
Pfdn6 RNAi
Pfdn6 RNAi
Pfdn6 RNAi
TBCE RNAi
CCT5 RNAi
CCT7 RNAi
G BL65365
H GD34204
I KK101541
J BL34537
K BL41818
L BL34931
M
Percentage of degenerated eye area
150
100
50
0
ns
***
GMR-Gal4>UAS-hTau^{V337M}
UAS-GFP
Pfdn4 RNAi (BL77412)
Pfdn5 RNAi (BL67815)
Pfdn5 RNAi (KK100796)
Pfdn5 RNAi (GD29812)
Pfdn6 RNAi (BL65365)
Pfdn6 RNAi (GD34204)
Pfdn6 RNAi (KK101541)
TBCE RNAi (BL34537)
CCT5 RNAi (BL41818)
CCT7 RNAi (BL34931)
GMR-Gal4>UAS-hTau^{V337M}

Figure_1

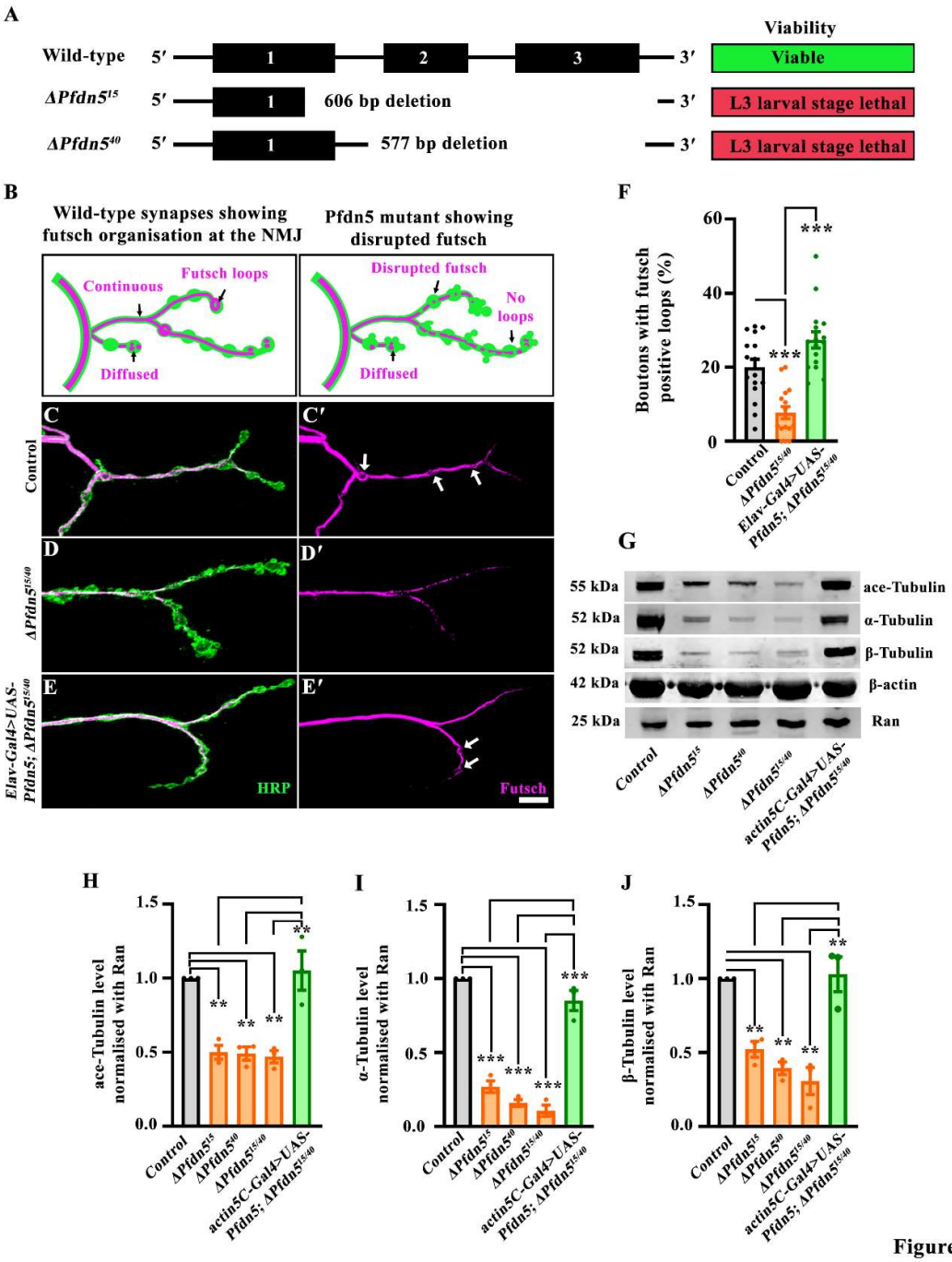
A
Viability
Wild-type
5′
1
2
3
3′
Viable
ΔPfdn5^15
606 bp deletion
L3 larval stage lethal
ΔPfdn5^40
577 bp deletion
L3 larval stage lethal
B
Wild-type synapses showing futsch organisation at the NMJ
Pfdn5 mutant showing disrupted futsch
Continuous
Futsch loops
Diffused
Disrupted futsch
No loops
Diffused
Control
ΔPfdn5^15/40
Elav-Gal4>UAS-Pfdn5; ΔPfdn5^15/40
C
C′
D
D′
E
E′
HRP
Futsch
F
Boutons with futsch positive loops (%)
Control
ΔPfdn5^15/40
Elav-Gal4>UAS-Pfdn5; ΔPfdn5^15/40
G
55 kDa
52 kDa
52 kDa
42 kDa
25 kDa
ace-Tubulin
α-Tubulin
β-Tubulin
β-actin
Ran
Control
ΔPfdn5^15
ΔPfdn5^40
ΔPfdn5^15/40
actin5C-Gal4>UAS-Pfdn5; ΔPfdn5^15/40
H
ace-Tubulin level normalised with Ran
I
α-Tubulin level normalised with Ran
J
β-Tubulin level normalised with Ran

Figure_2

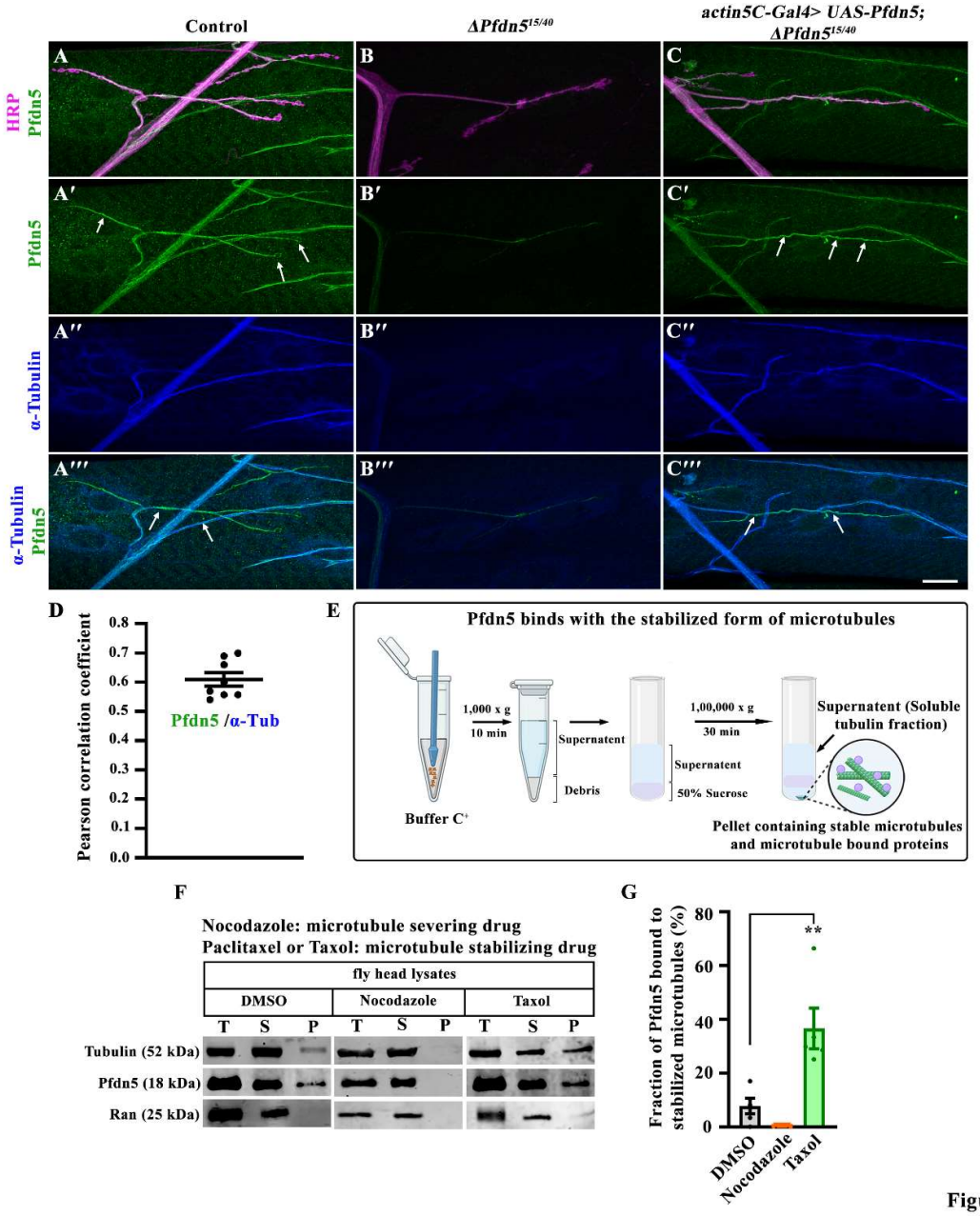
Control
ΔPfdn5^15/40
actin5C-Gal4> UAS-Pfdn5; ΔPfdn5^15/40
HRP
Pfdn5
α-Tubulin
α-Tubulin
Pfdn5
A
B
C
A′
B′
C′
A″
B″
C″
A‴
B‴
C‴
D
Pearson correlation coefficient
0.8
0.7
0.6
0.5
0.4
0.3
0.2
0.1
0.0
Pfdn5 /α-Tub
E
Pfdn5 binds with the stabilized form of microtubules
1,000 x g
10 min
Supernatent
Debris
1,00,000 x g
30 min
Supernatent
50% Sucrose
Supernatent (Soluble tubulin fraction)
Buffer C+
Pellet containing stable microtubules and microtubule bound proteins

F
Nocodazole: microtubule severing drug
Paclitaxel or Taxol: microtubule stabilizing drug
fly head lysates
DMSO
Nocodazole
Taxol
T S P T S P T S P
Tubulin (52 kDa)
Pfdn5 (18 kDa)
Ran (25 kDa)

G
Fraction of Pfdn5 bound to stabilized microtubules (%)
80
60
40
20
0
**
DMSO
Nocodazole
Taxol

Figure_3

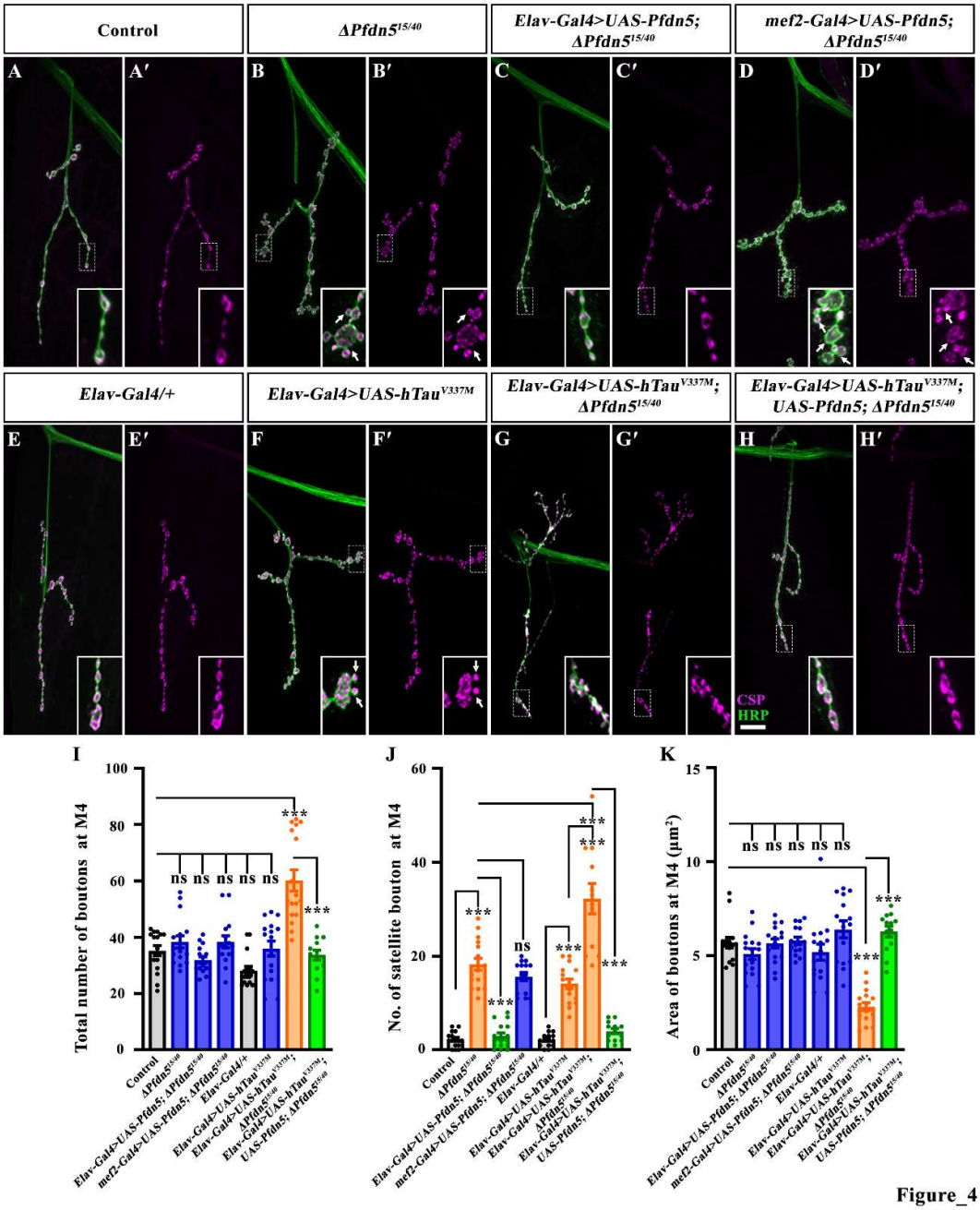
Control
ΔPfdn5^15/40
Elav-Gal4>UAS-Pfdn5; ΔPfdn5^15/40
mef2-Gal4>UAS-Pfdn5; ΔPfdn5^15/40
Elav-Gal4/+
Elav-Gal4>UAS-hTau^V337M
Elav-Gal4>UAS-hTau^V337M; ΔPfdn5^15/40
Elav-Gal4>UAS-hTau^V337M; UAS-Pfdn5; ΔPfdn5^15/40
CSP
HRP
Total number of boutons at M4
No. of satellite bouton at M4
Area of boutons at M4 (μm²)
ns
***

Figure_4

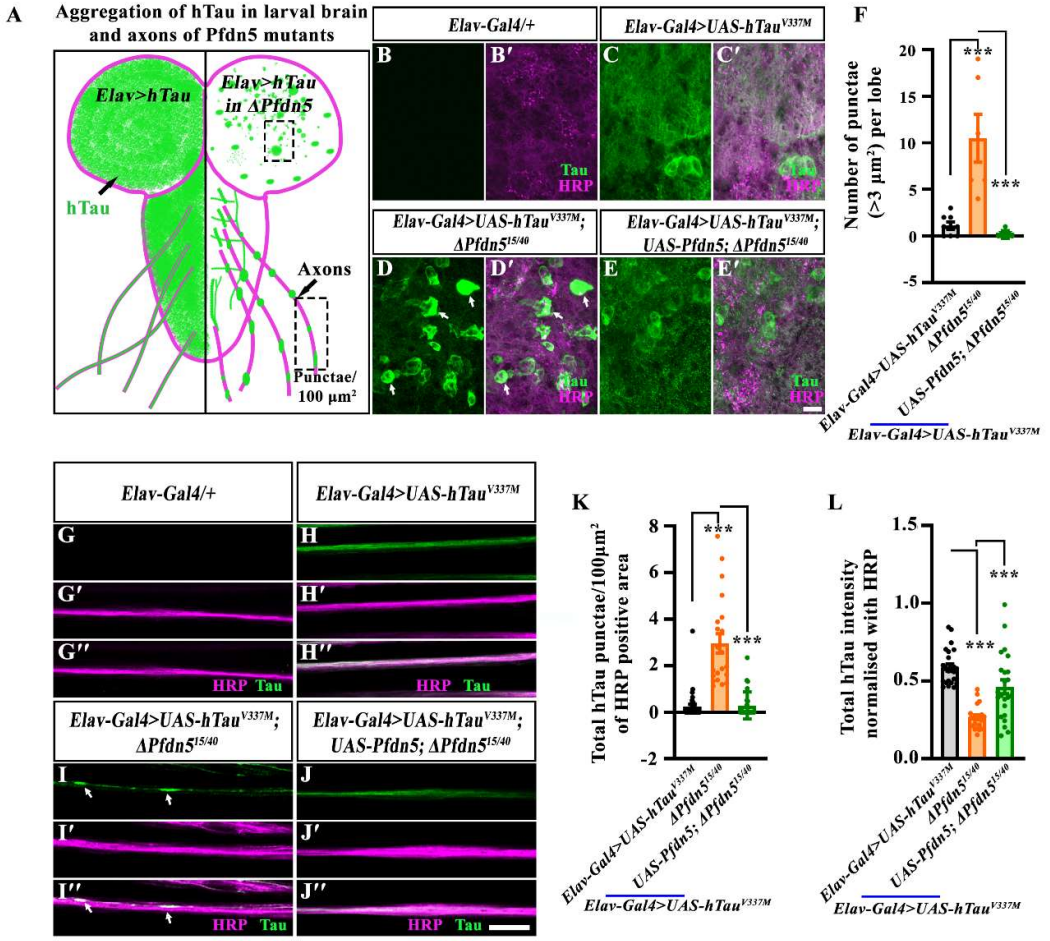
A
Aggregation of hTau in larval brain and axons of Pfdn5 mutants
Elav>hTau
Elav>hTau in ΔPfdn5
hTau
Axons
Punctae/ 100 μm²
Elav-Gal4/+
Elav-Gal4>UAS-hTauV337M
Elav-Gal4>UAS-hTauV337M; ΔPfdn515/40
Elav-Gal4>UAS-hTauV337M; UAS-Pfdn5; ΔPfdn515/40
Tau
HRP
F
Number of punctae (>3 μm²) per lobe
***
Elav-Gal4>UAS-hTauV337M
ΔPfdn515/40
UAS-Pfdn5; ΔPfdn515/40
K
Total hTau punctae/100μm² of HRP positive area
L
Total hTau intensity normalised with HRP

Figure_5

Age-dependent suppression of hTau^{V337M}-induced neurodegeneration by overexpression of Pfdn5 or Pfdn6

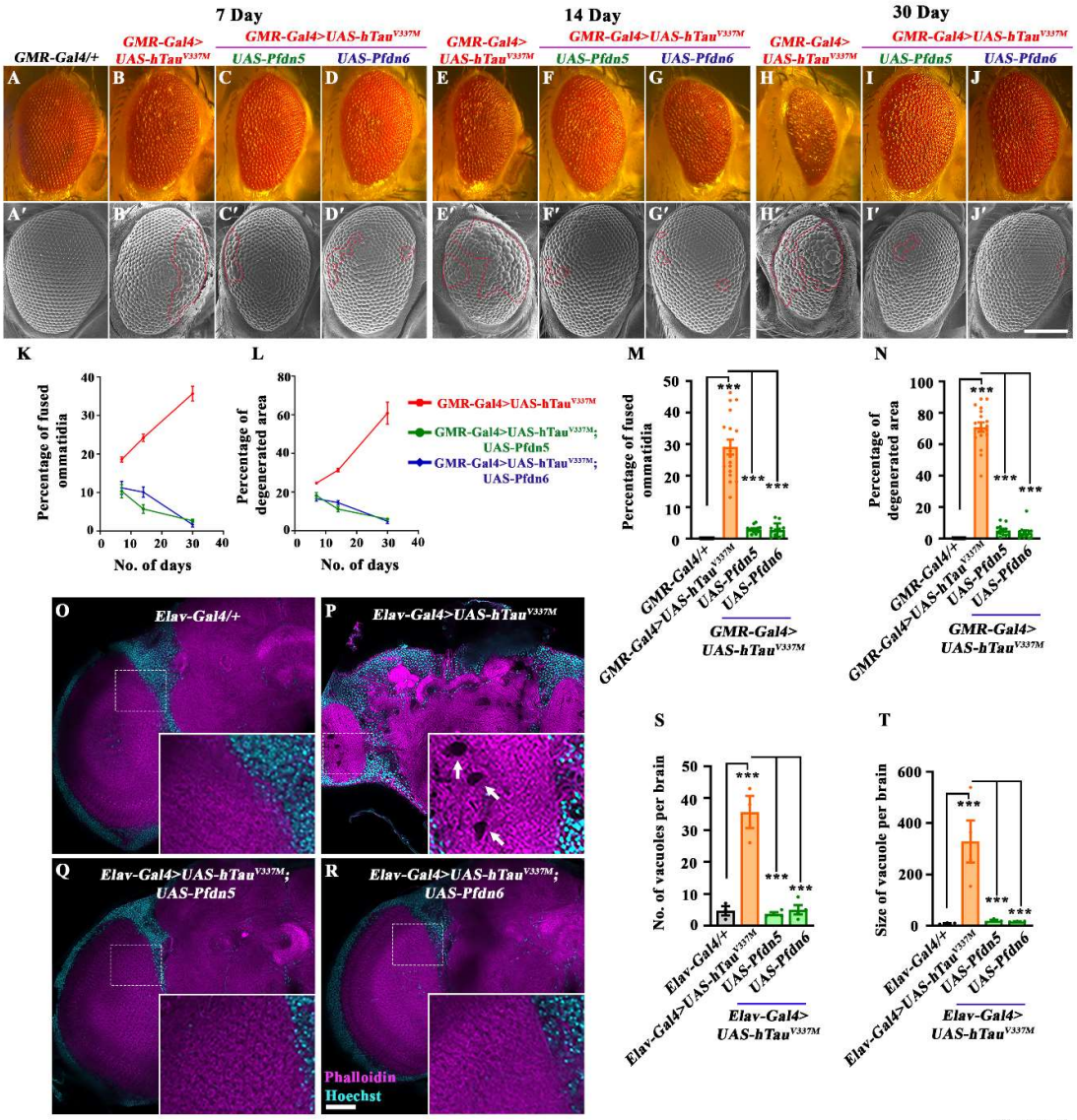

Figure_6

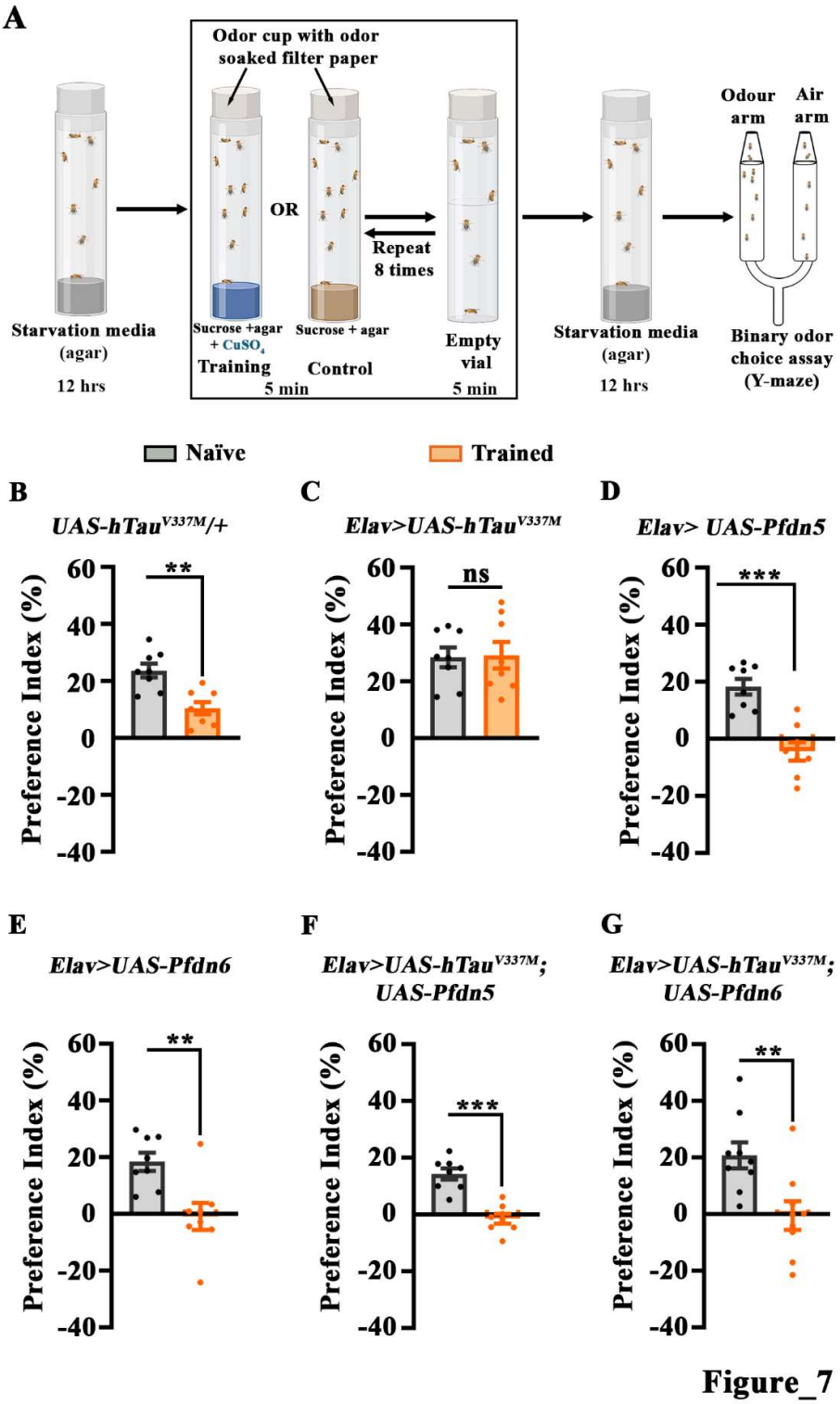
A
Odor cup with odor soaked filter paper
Starvation media (agar)
12 hrs
Sucrose +agar + CuSO4
Training
OR
Sucrose + agar
Control
5 min
Repeat 8 times
Empty vial
5 min
Starvation media (agar)
12 hrs
Odour arm
Air arm
Binary odor choice assay (Y-maze)
Naïve
Trained
B
UAS-hTauV337M/+
C
Elav>UAS-hTauV337M
D
Elav> UAS-Pfdn5
E
Elav>UAS-Pfdn6
F
Elav>UAS-hTauV337M; UAS-Pfdn5
G
Elav>UAS-hTauV337M; UAS-Pfdn6
Preference Index (%)
60
40
20
0
-20
-40
**
ns
***
**
***
**

Figure_7

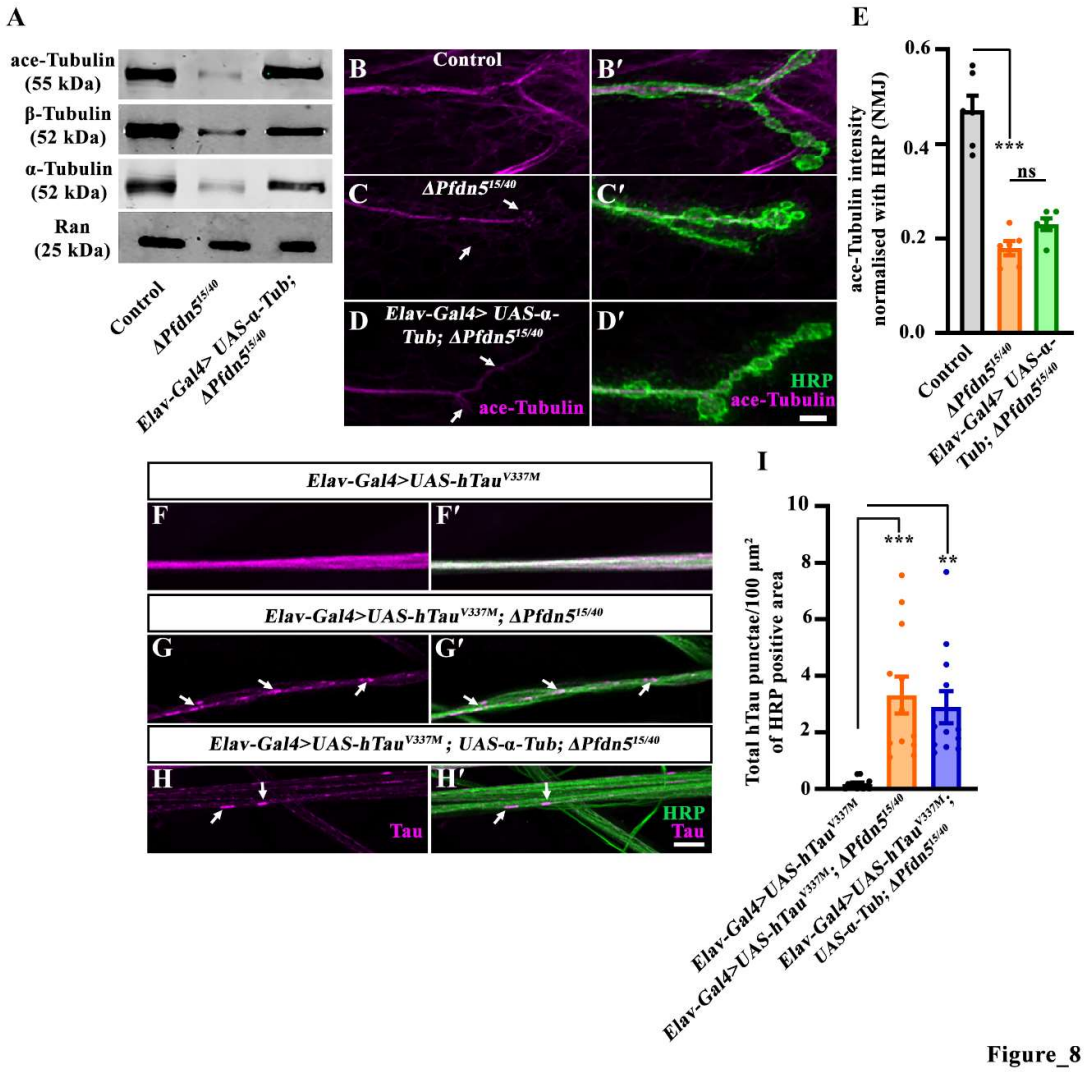
A
ace-Tubulin (55 kDa)
β-Tubulin (52 kDa)
α-Tubulin (52 kDa)
Ran (25 kDa)
Control
ΔPfdn5^15/40
Elav-Gal4> UAS-α-Tub; ΔPfdn5^15/40
B
Control
B′
C
ΔPfdn5^15/40
C′
D
Elav-Gal4> UAS-α-Tub; ΔPfdn5^15/40
ace-Tubulin
D′
HRP
ace-Tubulin
E
ace-Tubulin intensity normalised with HRP (NMJ)
0.6
0.4
0.2
0.0
***
ns
Control
ΔPfdn5^15/40
Elav-Gal4> UAS-α-Tub; ΔPfdn5^15/40
Elav-Gal4>UAS-hTau^V337M
F
F′
Elav-Gal4>UAS-hTau^V337M; ΔPfdn5^15/40
G
G′
Elav-Gal4>UAS-hTau^V337M ; UAS-α-Tub; ΔPfdn5^15/40
H
Tau
H′
HRP
Tau
I
Total hTau punctae/100 μm² of HRP positive area
10
8
6
4
2
0
***
**
Elav-Gal4>UAS-hTau^V337M
Elav-Gal4>UAS-hTau^V337M; ΔPfdn5^15/40
Elav-Gal4>UAS-hTau^V337M; UAS-α-Tub; ΔPfdn5^15/40

Figure_8

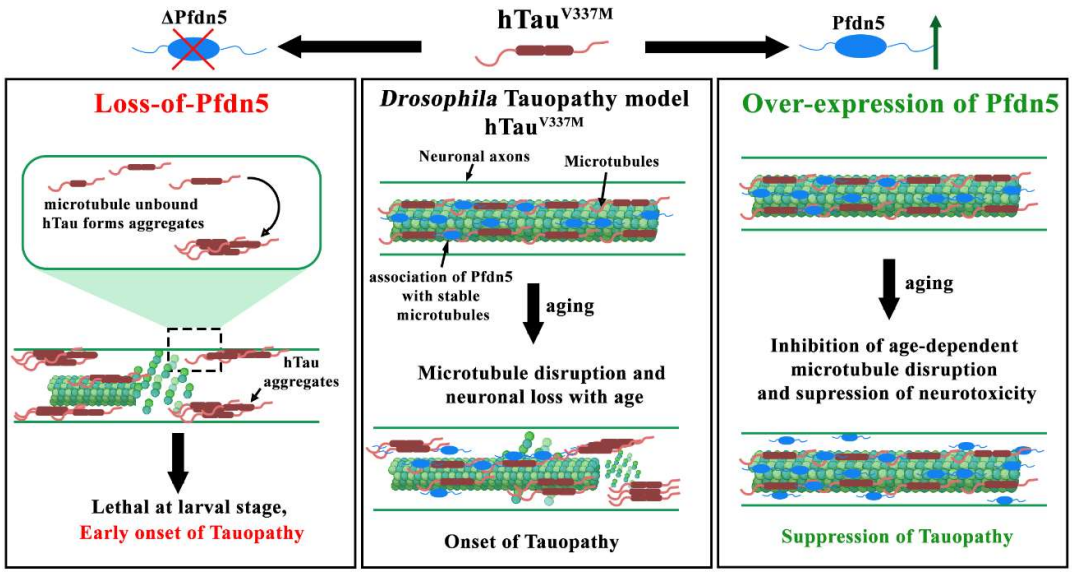
ΔPfdn5
hTau^{V337M}
Pfdn5
Loss-of-Pfdn5
microtubule unbound
hTau forms aggregates
hTau
aggregates
Lethal at larval stage,
Early onset of Tauopathy
Drosophila Tauopathy model
hTau^{V337M}
Neuronal axons
Microtubules
association of Pfdn5
with stable
microtubules
aging
Microtubule disruption and
neuronal loss with age
Onset of Tauopathy
Over-expression of Pfdn5
aging
Inhibition of age-dependent
microtubule disruption
and supression of neurotoxicity
Suppression of Tauopathy

Figure_9